Department of Chemistry and Materials Science

# Titania and silica based nanomaterials for decontamination and antibacterial applications

Henrika Granbohm

Aalto University

DOCTORAL DISSERTATIONS

Aalto University publication series
**DOCTORAL DISSERTATIONS** 159/2018

# Titania and silica based nanomaterials for decontamination and antibacterial applications

**Henrika Granbohm**

A doctoral dissertation completed for the degree of Doctor of Science (Technology) to be defended, with the permission of the Aalto University School of Chemical Engineering, at a public examination held at the lecture hall Ke2 of the school on 28th of September 2018 at 12 o'clock.

**Aalto University**
**School of Chemical Engineering**
**Department of Chemistry and Materials Science**
**Advanced and functional materials**

**Supervising professors**
Professor Simo-Pekka Hannula
School of Chemical Engineering
Aalto University, Finland

**Thesis advisors**
Professor Simo-Pekka Hannula
School of Chemical Engineering
Aalto University, Finland

**Preliminary examiners**
Professor Markku Leskelä
Department of Chemistry
University of Helsinki, FInland

PhD María del Puerto Morales (Senior Scientist)
Instituto de Ciencia de Materiales, Spain

**Opponents**
Dr. Simon R. Hall
School of Chemistry
University of Bristol, UK

Aalto University publication series
**DOCTORAL DISSERTATIONS** 159/2018



ISBN 978-952-60-8145-8 (printed)
ISBN 978-952-60-8146-5 (pdf)
ISSN 1799-4934 (printed)
ISSN 1799-4942 (pdf)
http://urn.fi/URN:ISBN:978-952-60-8146-5

Unigrafia Oy
Helsinki 2018

Finland

NORDIC ECOLABEL
441 697
Printed matter

**A! Aalto University**

# Abstract

**Aalto University, P.O. Box 11000, FI-00076 Aalto** www.aalto.fi

**Author**
Henrika Granbohm

**Name of the doctoral dissertation**
Titania and silica based nanomaterials for decontamination and antibacterial applications

**Publisher** School of Chemical Engineering

**Unit** Department of Chemistry and Materials Science

**Series** Aalto University publication series DOCTORAL DISSERTATIONS 159/2018

**Field of research** Materials Science

**Manuscript submitted** 5 June 2018 **Date of the defence** 28 September 2018

**Permission to publish granted (date)** 20 June 2018 **Language** English

☐ **Monograph** ☒ **Article dissertation** ☐ **Essay dissertation**

**Abstract**

The nanomaterials in this thesis are developed to counteract harmful organic pollutants and bacteria in our environment. Titania-based nanomaterials are prepared and the properties are examined for photocatalytic purposes to decontaminate waters with organic pollutants. Silica-silver nanomaterials are developed for antibacterial purposes.

Titania-based nanotubes and composites were developed for organic contaminants removal via photocatalysis. The nanotubes were prepared by chemical solution processing and rapid breakdown anodization (RBA) methods and further subjected to heat treatment. The chemical solution processing method yielded titanate-anatase mixed crystal structures, and anatase, rutile or brookite structures when using RBA. The heat treatment caused the tubular structure to collapse into rods and further into particles in both cases. The thermal stability of the tubular structure was higher for the titanate nanotubes compared to the nanotubes prepared by RBA. The surface area and amount of hydroxide functional groups reduced upon increasing heat treatment temperatures. The titania based composite consisted of four components, i.e., titania, graphene oxide, silver, and silver chloride. The photocatalytic efficiency was investigated using methylene blue (MB), methyl orange (MO) and rhodamine B (RhB) under UV and/ or sunlight irradiation. The photocatalytic decolorization of MB under UV light was reduced upon increased heat treatment temperatures for the titanate nanotubes, due to the reduced hydroxyl groups and surface area. Almost complete photocatalytic decolorization of MO and RhB was achieved using titania nanotubes under sunlight irradiation. The graphene oxide/titania/silver/silver chloride composites showed a high adsorptive capability of MB, due to the abundance of hydroxyl functional groups. The photocatalytic decolorization reached 55 % under UV-light irradiation and increased by ca 80 % with the addition of graphene oxide to the titania/silver/silver chloride composites. The silica-silver composites were prepared by a modified Stöber method. The silica-silver composite powders were subjected to heat treatment to study the silver nanoparticle growth and to determine the activation energy for silver particle growth. The mean size of the silver particles grew with increasing heat treatment temperature. The activation energy for silver particle growth was determined as 0.14 eV, and the growth took place via diffusion and Ostwald ripening. The feasibility of a prolonged silver release from the composites was investigated via dissolution tests, which showed a prolonged release for at least 7 days' time. One silica-silver composite was chosen for antibacterial tests for wound dressing applications. The silica-silver composite hindered the growth of both methicillin-resistant Staphylococcus aureus (MRSA) and Escherichia coli. The composite was also impregnated in a gauze to simulate a wound dressing and hindered the bacterial growth more efficiently than a commercial silver containing gauze. The antibacterial mechanism was elucidated for MRSA, where the silver ions eventually caused the loss of bacterial membranes.

**Keywords** titania, nanotubes, photocatalysis, silica, silver, antibacterial, particle growth

**ISBN (printed)** 978-952-60-8145-8 **ISBN (pdf)** 978-952-60-8146-5

**ISSN (printed)** 1799-4934 **ISSN (pdf)** 1799-4942

**Location of publisher** Helsinki **Location of printing** Helsinki **Year** 2018

**Pages** 183 **urn** http://urn.fi/URN:ISBN:978-952-60-8146-5

**Aalto-universitetet**

**Aalto-universitetet, PB 11000, 00076 Aalto** www.aalto.fi

# Sammandrag

**Författare**
Henrika Granbohm

**Doktorsavhandlingens titel**
Bearbetning och egenskaper av titandioxid och kiseldioxid nanomaterial

**Utgivare** Högskolan för kemiteknik

**Enhet** Institutionen för kemi och materialvetenskap

**Seriens namn** Aalto University publication series DOCTORAL DISSERTATIONS 159/2018

**Forskningsområde** Materialteknik

**Inlämningsdatum för manuskript** 05.06.2018 **Datum för disputation** 28.09.2018

**Beviljande av publiceringstillstånd (datum)** 20.06.2018 **Språk** Engelska

☐ **Monografi** ☒ **Artikelavhandling** ☐ **Essäavhandling**

**Sammandrag**
Nanomaterialen i denna avhandling utvecklades för förebyggandet av skadliga organiska föroreningar och bakterier i vår omgivning. Nanomaterial baserade på titandioxid framställdes och egenskaperna av dessa undersöktes för dekontamination av förorenade vatten via fotokatalys. Nanomaterial av silikondioxid-silver utvecklades för antibakteriella syften.
Nanorör baserade på titandioxid framställdes genom en kemisk lösningsmetod och en snabb sönderdelningsanodiseringsmetod (RBA) och utsattes för värmebehandling. Den kemiska lösningsmetoden gav blandade titanat-anatas kristallstrukturer och vid användning av RBA uppstod strukturer utav anatas, rutil eller brookit. Värmebehandlingen förorsakade kollaps av den rörformiga strukturen till stavar och till partiklar med ytterligare värmebehandling. Den rörformiga strukturens termiska stabilitet var högre för nanorören av titanat jämfört med de nanorör som framställdes med RBA. Arean för och mängden hydroxid-grupper minskade för nanorören vid högre värmebehandlingstemperatur. Den titandioxidbaserade kompositen bestod av fyra komponenter: titandioxid, grafenoxid (GO), silver och silverklorid. Den fotokatalytiska effektiviteten undersöktes med hjälp av metylenblå (MB), metylorange (MO) och rhodamin B (RhB) under bestrålning UV- och / eller solljus. Den fotokatalytiska avfärgningen av MB under UV-ljus minskade vid ökad värmebehandlingstemperatur av titanatnanorören, på grund av den reducerade arean och mängden av hydroxidgrupper. Nästan fullständig fotokatalytisk avfärgning av MO och RhB uppnåddes med användning av titandioxidnanorör under solljus. GO/titandioxid/silver/silverklorid-kompositerna uppvisade hög adsorptionsförmåga hos MB, p.g.a. överflöd av hydroxidgrupper. Den fotokatalytiska avfärgningen uppnådde 55 % under UV-ljusbestrålning och ökade med ca 80 % med tillsatsen av GO till titanoxid/silver/silverklorid-kompositerna. Kompositpulver av kiseloxid-silver framställdes med en modifierad Stöber-metod. Dessa kompositpulver av kiseldioxid-silver utsattes för värmebehandling för att undersöka tillväxten av nanopartiklar av silver och för att bestämma aktiveringsenergin för tillväxten av dessa partiklar. Medelstorleken av silver partiklarna växte med ökande värmebehandlingstemperatur. Aktiveringsenergin för silverpartikeltillväxt bestämdes som 0,14 eV och tillväxten skedde genom diffusion och Ostwald-mogning. Genomförbarheten av en förlängd frisättning av silver från kompositerna undersöktes genom upplösningstester, vilket visade en långvarig frisättning under åtminstone 7 dagar. En kiseldioxid-silverkomposit valdes för antibakteriella tester för förbandstillämpningar. Kiseldioxid-silverkompositen hindrade tillväxten av både det meticillinresistenta Staphylococcus aureus (MRSA) och Escherichia coli. Kompositen impregnerades också i en gasbinda för att simulera ett förband. Den hindrade bakterietillväxten effektivare än en kommersiell gasbinda som innehöll silver. Den antibakteriella mekanismen av silver mot MRSA klargjordes, då silverjonerna slutligen förorsakade förlust av bakteriemembranen

**Nyckelord** titandioxid, nanorör, fotokatalys, kiseldioxid, silver, antibakterisk, partikeltillväxt

**ISBN (tryckt)** 978-952-60-8145-8 **ISBN (pdf)** 978-952-60-8146-5

**ISSN (tryckt)** 1799-4934 **ISSN (pdf)** 1799-4942

**Utgivningsort** Helsingfors **Tryckort** Helsingfors **År** 2018

**Sidantal** 183 **urn** http://urn.fi/URN:ISBN:978-952-60-8146-5

# Preface

The research in this thesis was carried out between the years 2014-2018 at the Department of Chemistry and Materials Science, School of Chemical Engineering at Aalto University. The research was funded by the Aalto Energy Efficiency Research Programme through the EXPECTS (Exploiting Scale Effects for High Efficiency Thermal Systems) project. The financial support of the Technology Industries of Finland Centennial Foundation and the Foundation for Aalto University Science and Technology is greatly acknowledged. In addition, I would like to thank the LUMA Center of Aalto, now known as Aalto University Junior (former LUMARTS laboratory) for my time there.

I would like to address my appreciation to my supervisor, Professor Simo-Pekka Hannula. I am incredibly thankful for the opportunity to work towards a doctoral degree in your group. The support and inspiration from Prof. Hannula has now reached the goal of graduation.

This thesis has involved support from many people. I appreciate all my co-authors for their contribution and I am grateful for having the opportunity to collaborate with all of them. I want to thank Dr. Yanling Ge for her extraordinary knowledge in TEM. Saima Ali is gratefully acknowledged as my hard working co-author. I have been fortunate to have Saima as my co-author and friend, where we have had long discussions both work associated and private. Saima has cheered me up so many times. Thank you. I am grateful to have Frans Nilsén as co-author, collegue and friend. Nothing is better than a little healthy competition in writing the thesis and finding motivation together. Listening to "Tosche Station" on repeat also helps! Thank you Joonas for accompanying me on the refreshing walks and "dream house" hunting. I want to thank my other co-workers Shima Moosahkani, Ilkka Penttinen and Qian Chen. I also want to thank my former collegues Juha Larismaa, Erkin Cura, Ilkka Aaltio and Ajai Iyer for keeping me company and helping me keep my sanity. Thank you Vasuki for the suggestions to improve the flow in the thesis and for the language check.

I want to thank my family. Tack mamma och pappa för att ni alltid lyssnat och stött mig. Det är inte möjligt att lista allt jag är tacksam för, så tack Alexandra, Richard och Fanny för allting. Ni är de bästa syskon jag någonsin kunde önska mig. Tack Fanny för att du rättade språket i mitt abstrakt.

Lastly, I want to thank my rock and the love of my life, Ville. Kiitos että olet tukenut ja kuunnellut minua kun olen sitä tarvinnut.

Espoo, August 23, 2018,

Henrika Granbohm

# Contents

# List of Publications

This thesis consists of an overview and of the following publications which are referred to in the text by their Roman numerals.

**I** Saima Ali, Henrika Granbohm, Yanling Ge, Vivek K. Singh, Frans Nilsén, Simo-Pekka Hannula. Crystal structure and photocatalytic properties of titanate nanotubes prepared by chemical processing and subsequent annealing. *Journal of Materials Science*, 51 (15) pp. 7322-7335, doi: 10.1007/s10853-016-0014-5, May 2016.

**II** Saima Ali, Henrika Granbohm, Jouko Lahtinen, Simo-Pekka Hannula. Titania nanotubes prepared by rapid breakdown anodization for photocatalytic decolorization of organic dyes under UV and natural solar light. *Nanoscale Research Letters*, 13, 179, https://doi.org/10.1186/s11671-018-2591-5, June 2018.

**III** Henrika Granbohm, Kati Kulmala, Ajai Iyer, Yanling Ge, Simo-Pekka Hannula. Preparation and Photocatalytic Activity of Quaternary GO/$TiO_2$/Ag/AgCl Nanocomposites. *Water, Air & Soil Pollution*, 228 (4) pp. 127, doi: 10.1007/s11270-017-3313-9, April 2017.

**IV** Henrika Granbohm, Juha Larismaa, Saima Ali, Leena-Sisko Johansson, Simo-Pekka Hannula. Control of the size of silver nanoparticles and release of silver in heat treated $SiO_2$-Ag composite powders. *Materials*, 11 (1), 80, doi: 10.3390/ma11010080, January 2018.

**V** Dina A. Mosselhy, Henrika Granbohm, Ulla Hynönen, Yanling Ge, Airi Palva, Katrina Nordström, Simo-Pekka Hannula. Nanosilver–silica composite: Prolonged antibacterial effects and bacterial interaction mechanisms for wound dressings. *Nanomaterials*, 7 (9), 261, doi: 10.3390/nano7090261, September 2017.

# Author's Contribution

### Publication I: "Crystal structure and photocatalytic properties of titanate nanotubes prepared by chemical processing and subsequent annealing"

The author and M. Sc. (tech.) Ali defined the research plan under the guidance of Prof. Hannula. M. Sc. (tech.) Ali prepared the TNT materials and carried out the structural characterization (TEM, FTIR, XRD, TGA, Raman, UV-vis diffuse reflectance and nitrogen adsorption–desorption) and the interpretation of these results. The author performed the photocatalytic experiments, analyzed the results associated with photocatalysis and wrote the photocatalytic parts of the publication. M. Sc. (tech) Nilsén assisted with the EDX characterization. Dr. Ge helped with the TEM characterization and Dr. Singh assisted with the Raman characterization.

### Publication II: "Titania nanotubes prepared by rapid breakdown anodization for photocatalytic decolorization of organic dyes under UV and natural solar light"

M. Sc. (tech.) Ali and the author defined the research plan under the guidance of Prof. Hannula. M. Sc. (tech.) Ali and the author performed the experimental parts, the analysis of the results and the preparation of the publication together. M. Sc. (tech.) Ali performed TEM, DRS, XRD, FTIR, and photocurrent measurements. The author conducted the photocatalytic experiments by M. Sc. (tech.) Ali. The author interpreted the photocatalytic results and wrote the photocatalytic part in the article. The author performed the EIS and PL measurements and analysis. The author and M. Sc. (tech.) Ali discussed the interpretation of the results continuously. Dr. J. Lahtinen performed the XPS measurement and analysis. All authors revised the manuscript.

## Publication III: "Preparation and Photocatalytic Activity of Quaternary GO/$TiO_2$/Ag/AgCl Nanocomposites"

The author defined the research plan under the guidance of Prof. Hannula. The author performed the experimental part together with M. Sc. (tech.) Kulmala. The author was responsible for the analysis of the results and the preparation of the publication. Dr. Iyer carried out the Raman characterization and provided guidance on the analysis. Dr. Ge was responsible for TEM analysis and advised on the analysis for the publication.

## Publication IV: "Control of the size of silver nanoparticles and release of silver in heat treated $SiO_2$-Ag composite powders"

The author was responsible to finalize the experiments, to interpret the experimental results and to write the publication under the guidance of Prof. Hannula. The author and M. Sc. (tech.) Larismaa performed the synthesis of the powders. M. Sc. (tech.) Larismaa performed SEM and TEM imaging and the analysis of the Ag particle sizes, as well as, some UV-vis characterization. Further SEM and TEM analysis was made by the author. Dr. Johansson performed the XPS analysis and participated in writing the XPS analysis in the publication. M. Sc. (tech.) Ali performed the nitrogen adsorption-desorption experiments, FTIR characterization and participated in writing the introduction. The author, M. Sc. (tech.) Larismaa and Prof. Hannula reviewed the particle growth and interpreted the results. The author was responsible for the dissolution experiments and the characterization of the dissolved powders.

## Publication V: "Nanosilver–silica composite: Prolonged antibacterial effects and bacterial interaction mechanisms for wound dressings"

Dina A. Mosselhy designed and performed all the antibacterial tests against *E. coli* (in Aalto University) and MRSA (in University of Helsinki) under the supervision of Katrina Nordström and Airi Palva, respectively. Henrika Granbohm prepared the nanomaterials and Dina A. Mosselhy performed the Ag leaching experiment from the composite under the supervision of Simo-Pekka Hannula. Dina A. Mosselhy and Ulla Hynönen interpreted the antibacterial results. Henrika Granbohm characterized the nanomaterials by XRD, SEM, and TEM. Yanling Ge performed further TEM imaging and analyses (electron diffraction pattern, HRTEM, and EDX) of the composite, and TEM and STEM analyses of the composite-treated bacterial cells. Dina A. Mosselhy interpreted the characterization results, Ag leaching results, and the TEM and STEM data of the composite-treated bacterial cells. Dina A. Mosselhy wrote the manuscript. All the authors revised the manuscript with eminent inputs contributed by Ulla Hynönen. All the authors approved the final version of the manuscript.

# Nomenclature

| | |
|---|---|
| AAO | Anodic aluminium oxide |
| AES | Atomic emission spectroscopy |
| ALD | Atomic layer deposition |
| AO7 | Acid orange 7 |
| BET | Brunauer-Emmet-Teller |
| BJH | Barrett-Joyner-Halenda |
| CFU | Colony forming unit |
| CSD | Commercial Ag-containing dressing |
| CTAB | Hexadecyltrimethylammonium bromide |
| D | Particle size (diameter) |
| DI | De-ionized water |
| DNA | Deoxyribonucleic acid |
| DSSC | Dye-sensitized solar cell |
| *E.coli* | Escherichia coli |
| EDX | X-ray energy dispersive spectrometry |
| EIS | Electrochemical impedance spectroscopy |
| FEG-SEM | Field emission gun scanning electon microscope |
| FFT | Fast Fourier transform |
| FTIR | Fourier transform infrared spectroscopy |
| GO | Graphene oxide |
| GrO | Graphite oxide |
| HRTEM | High-resolution transmission electron microscopy |
| ICDD | International centre of diffraction data |
| ICP | Inductively coupled plasma |
| IPCE | Incident photon to photocurrent efficiency |
| IZ | Inhibition zone |

| | |
|---|---|
| LB | Luria-Bertani |
| LSPR | Localized surface plasmon resonance |
| MB | Methylene blue |
| MHA | Mueller-Hinton agar |
| MHB | Mueller-Hinton broth |
| MIC | Minimum inhibitory concentration |
| MO | Methyl orange |
| MRSA | Methicillin-resistant *Staphylococcus aureus* |
| NP | Nanoparticle |
| P25 | Degussa P25, a commercial $TiO_2$ photocatalyst |
| PL | Photoluminescence spectroscopy |
| PVP | Poly(N-vinyl-2-pyrrolidone) |
| $Q_A$ | Activation energy |
| RBA | Rapid breakdown anodization |
| RGO | Reduced graphene oxide |
| RhB | Rhodamine B |
| RT | Room temperature |
| SAED | Selected area electron diffraction |
| SEM | Scanning electron microscope |
| SERS | Surface enhanced Raman spectroscopy |
| STEM | Scanning transmission electron microscopy |
| SPR | Surface plasmon resonance |
| TEM | Transmission electron microscope |
| TEOS | Tetraethyl orthosilicate |
| TGA | Thermogravimetric analysis |
| TG-DTA | Thermogravimetric-differential thermal analysis |
| TNT | Titania nanotube |
| UV | Ultraviolet |
| XPS | X-ray photoelectron spectroscopy |
| XRD | X-ray diffraction |

# 1. Introduction

An article in Business Insider caught my attention recently. As a millennial myself, the title was noteworthy: "The 10 biggest problems in the world today, according to millennials". While climate change and political stability seem to be the top priority of this generation, a significant percentage of the developing countries still list food and water security and well being as a primary concern [1]. I have been lucky so far: I grew up healthy and surrounded by clean water in the beautiful Finnish archipelago. This is definitely nothing anyone should take for granted. To be and to stay healthy will become increasingly difficult with the existing and increasing antibiotic-resistant bacteria and the polluted waters surrounding us.

Clean water is a vital resource for healthy living. Unfortunately, the clean water supplies on Earth are threatened by pollution, both intentional and accidental. Several water purification techniques including filtration, sedimentation and flocculation exist. Most of these techniques however require expensive and bulky equipment that are often unavailable in the developing and low income nations. Photocatalysts have gained increasing interest in the recent years as potential point of use water purification method [2]. Photocatalysts can be defined as materials, which accelerate chemical reactions by light irradiaton, without themselves undergoing a chemical change or depletion.

In this thesis, photocatalysts are investigated for organic contaminants removal under UV- and natural sunlight irradiation. Titanium dioxide, $TiO_2$, was chosen as the base for the photocatalytic investigations due to its already high photocatalytic efficiency and tunability. The upside of photocatalysts is that they only need a light source, such as sunlight or an indoor light fixture, to degrade pollutants. However, there are several limiting factors with $TiO_2$ of which the most prominent is that $TiO_2$ can only use UV-light to degrade pollutants. It is generally known that UV-light is only a small part of the sunlight spectrum and to prepare more efficient photocatalysts it is crucial to be able to use a wider range of light for the degradation, thus the light absorption of $TiO_2$ needs to be tuned. For this purpose, titania nanotubes, titanate nanotubes and a quaternary nanocomposite of graphene oxide/$TiO_2$/silver/silver chloride were investigated in this thesis.

While clean water forms the basis of a healthy life, staying healthy requires the ability to overcome minor injuries that are common in the day to day life. Accidental scrapes and paper cuts are considered insignificant injuries these days, but the constant misuse of antibiotics might set us back to a pre-antibiotic era where the wound infection of these insignificant injuries might cost lives.. The misuse of antibiotics render bacteria antibiotic-resistant, to form so-called superbugs. There are already a few superbugs, the most notable being MRSA (Methicillin-Resistant *Staphylococcus aureus*), which is common in hospitals where people have open wounds. This thesis presents a $SiO_2$-Ag composite for wound dressings, to reduce the use of topical antibiotics on wounds.

This thesis has four chapters. After a brief description of the studied materials and applications, this chapter presents the background of the investigated materials, i.e., $TiO_2$ and $SiO_2$ based nanomaterials and their applications, and the aim of the conducted research. The second chapter deals with the preparation of the $SiO_2$ and $TiO_2$ materials used and describes the equipment and methods used to study the properties of the materials. The third chapter presents the significant results of this thesis and includes a comprehensive discussion of the materials. The last chapter compiles the thesis and concludes the obtained results. The significance of the results for future development and applications are further evaluated.

## 1.1 Properties of titanium dioxide materials and photocatalysis

The research on titania materials is vast: it extends from nanoparticles (NPs) to nanotubes to films and other titania structures. These titania materials are used in applications such as dye-sensitized solar cells (DSSC) [3], gas-sensors [4], fabrics [5], coatings [6], and photocatalysis [7]. The focus in this thesis is on the application of photocatalysis and more specifically on the photocatalytic removal of unwanted organic contaminants. However, photocatalysts are also used for heavy metals removal [8], water splitting [9, 10], and self-cleaning surfaces [11]. The versatility of titania materials lies in the differences in crystal structure, morphology and preparation methods. This section introduces titanium dioxide ($TiO_2$, titania) materials, specifically titania and titanate nanotubes, and titania composites. Their basic properties, crystal structure and overview of literature on preparation and applications are briefly discussed.

There are three main types of titanium dioxide structures, namely anatase, rutile, and brookite. Anatase and rutile are the more common phases and anatase is usually found in particles up to 11 nm and rutile in particles larger than 35 nm. Brookite is a rarer structure and is usually found in 11-35 nm sized particles [12]. Anatase and rutile are typical n-type semiconductors due to oxygen vacancies in the crystal structure, and thus also display $Ti^{3+}$ sites. The band gaps of anatase, rutile and brookite are 3.2 eV [13], 3.0 ev [7] and 3.1-3.4 eV [13], respectively. The size of the band gap has a huge role when considering the application field of photocatalysis.

Titania is one of the most commonly used semiconductor photocatalysts. Photocatalysis is the catalysis of a photochemical reaction on a solid surface, here on a titania surface [12]. For photocatalytic water purification to take place, two reactions are required: oxidation and reduction. When the light hits the photocatalyst, electrons and holes are created, i.e. charge carriers or electron/hole pairs. The light photoinduces electrons ($e^-$) to a forbidden state, simultaneously generating holes ($h^+$). Fig. 1.1 illustrates the electron-hole pair created by the incident light taking different routes: i) they can recombine in the bulk or at the surface of the photocatalyst via trap states or band to band transitions, ii) form an oxidized state on the surface of the photocatalyst, which can be disadvantageous for the efficiency or iii) separate undergoing further oxidation-reduction reactions, which generate, for example, free radicals [14]. These electrons and holes which do participate in the redox reactions are the ones that have migrated to the surface of the photocatalyst particle and react with the adsorbed acceptor and donor, as shown in Fig. 1.1.

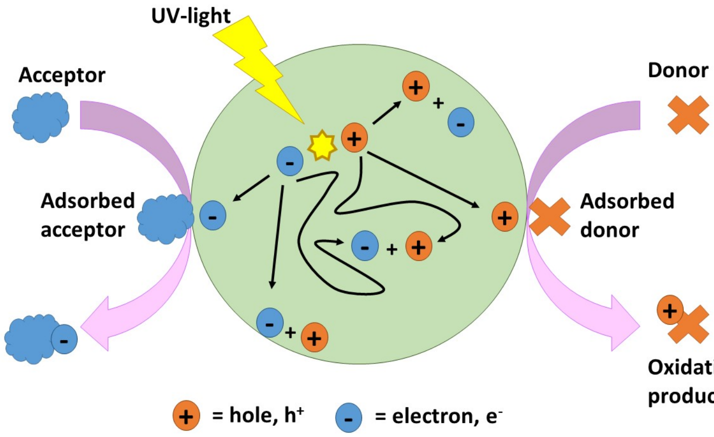


**Figure 1.1.** The major processes involved in photocatalysis. Reproduced after [14].

The photocatalytic activity of titania is affected by crystal structure (anatase/rutile), particle size and distribution, surface area, and surface functional groups [12]. These properties have a huge impact on the charge carrier formation, redox reactions and the adsorption and desorption processes. Attempts at improving the photocatalytic efficiency have been made by enhancing these properties, as an example, reducing the particle size to increase surface area.

One of the studied titania photocatalyst material is the commercially available Degussa P25 titania nanopowder. Degussa P25, or simply P25, consists of anatase and rutile in a ratio between 70:30 to 80:20, but other ratios are also reported [15]. P25 is the hydrolysis product of ($TiCl_4$) in a hot flame. The 21 nm sized nanoparticles of P25 has a surface area of 35 to 65 $m^2g^{-1}$ [16], which is neither high nor low considering nanomaterials. The photocatalytic efficiency of new photocatalyst materials is usually compared to Degussa P25, due to the high photocatalytic efficiency of P25. However, Degussa P25 is a controversial material since scientists are not in unison why the efficiency is so high. Speculations are that, it is due to charge separation and hindering of charge recombination in the mixed phase powder [17], however, others disagree [15].

Efforts are made to improve the photocatalysts even further, even though P25 is an efficient photocatalyst. The focus then lies on the reduction of the band gap, i.e., from the typical range of 3.0-3.4 eV for titania to smaller band gap values, in order to extend the efficient light range to the visible light range. The band gap can be reduced by forming different structures of titania, such as nanotubes [9, 10, 18], doping the titania structure with non-metals [9, 19], coupling titania with noble metals [20] or metal oxides [21], or by forming composite structures [22, 23].

### 1.1.1 Titania nanotubes

The one-dimensional titania nanotube (TNT) has attracted much attention in the recent years. Titania nanotubes are an attractive material due to their electrical and optical properties and the high specific surface area [24]. It is crucial to have a large surface area in many application fields, such as photocatalysis, and nanotubular structures or even nanorods may provide this [7].

TNTs are prepared by hydrothermal synthesis [25], chemical processing [26], electrochemical anodization [7] and template-based methods [27]. The hydrothermal synthesis was introduced by Kasuga *et al.* [25] in 1998. Typically, a titania powder, e.g. Degussa P25, is treated with 10 M NaOH in an autoclave for 1-2 days at 100-180 °C. The elevated temperature and alkaline treatment assist the formation of tubes. The resulting nanotubes powder is then washed with dilute HCl. The chemical processing method is similar to the hydrothermal method, and was also introduced by Kasuga *et al.* [26]. In chemical solution processing, titania powder is dispersed in concentrated NaOH at 110 °C for 20 h in either a closed glass vessel or under reflux to hinder evaporation. The resulting powder is first washed with water, followed by dilute HCl. The formation of the TNTs involves delamination of titania layers forming sheets from the precursor titania powder during the alkaline treatment. Subsequently, these sheets roll up to form the tubular structure. Whether the sheets roll up during the alkaline treatment or during the washing process may depend on the experimental conditions, as reports have been published supporting both [26, 28, 29]. The crystal structure of the formed nanotubes depends strongly on the parameters used during the chemical processing. Numerous titanate structures have been reported for the as-synthesised tubes, for example, $H_2Ti_3O_7$ [30], $Na_2H_2Ti_2O_4(OH)_2$ [31], $Na_2Ti_3O_7 \cdot H_2O$ [32] and $Na_xH_{2-x}Ti_2O_5 \cdot H_2O$ [33], but anatase [34] has also been reported. The processing parameters such as temperature, time, NaOH and HCl concentration and annealing of the tubes can be optimized for the desired TNT properties [28, 35, 36].

Another way of preparing titania nanotubes is through electrochemical anodization. Electrochemical anodization is performed in an electrolyte, using a Ti-substrate as the anode, Pt as the cathode and applying a suitable voltage, which forms a highly self-organized nanotube array as a film on the Ti-substrate [7]. In 1999, Zwilling *et al.* [37] introduced anodization in an electrolyte containing HF. Nowadays, the development of electrochemical anodization is divided into four generations, of which the first is anodization in HF electrolytes with 500 nm tube lengths [38]. The second generation is considered as using buffered electrolytes, i.e. pH controlled electrolytes, to increase the length of the nanotube array to micrometer size [39, 40]. Non-aqueous, polar, organic electrolytes were examined in the third generation to obtain even longer tubes up to hundreds of micrometers with a smooth surface [41]. Lately, research has focused on fluoride-free electrolytes and fast anodization [18]. The fast anodization method is called rapid breakdown anodization (RBA) and usually involves chloride or perchlorate containing electrolytes and can form tens to several hundred nanometers long tubular bundles within seconds of applying a voltage [18, 42]. The downside is that the nanotubes prepared by RBA have an absence of geometry control and a random distribution of the formed TNTs, however, the upside is that these RBA TNTs are fast and easy to make in larger quantities [24]. All anodized titania nanotubes are closed at the Ti-substrate end and open at the other end, as shown in Fig. 1.2. The thrid generation of anodized TNTs in Fig. 1.2a have a smooth surface due to the etching properties of fluoride in the ethylene glycol electrolyte, whereas the TNTs prepared by RBA in Fig. 1.2b have a rougher surface when prepared in the presence of chlorine ions in a perchloric acid-ethylene glycol electrolyte.

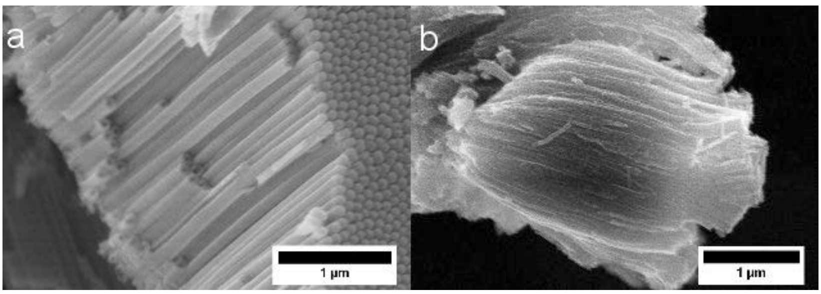


**Figure 1.2.** SEM images of a) anodized TNTs and b) TNTs prepared by RBA. Courtesy of Saima Ali.

Template-based methods are, as the name suggests, based on using a template to form the nanotubular film. The template-based methods require multiple steps for nanotubes preparation; i) formation of the template, ii) deposition of titania, iii) removal of the top layer of deposited titania, and iv) etching of the template [27]. One of the classic templates is anodic aluminum oxide (AAO), which can be prepared with highly defined order and pore distance [43]. The AAO is then filled or deposited with titania, which can be achieved for e.g. by sol-gel [44] or atomic layer deposition (ALD) [27].

For practical applications of TNTs in powder form, it is important to be able to produce TNT powders in larger quantities. Therefore, chemical processing methods and RBA are the most practical methods to produce larger quantities of TNTs, especially for photocatalytic purposes, although a number of studies have also investigated anodized TNT arrays. The photocatalytic removal of organic contaminants involves decolorization or decompositions of dyes, such as Methylene Blue (MB) [45, 46], Rhodamine B (RhB) [47, 48], Methyl Orange (MO) [47, 49], and Acid Orange 7 (AO7) [50] but the photocatalytic degradation is also probed with phenols [51, 52]. As the band gap of $TiO_2$ is in the UV-light range many investigations have been made under UV-light irradiation [45, 48, 50], but also under visible light [53] or simulated solar light [47].

The crystal structure of the TNTs affects the photocatalytic efficiency, but it also correlates with the band gap, surface area, and surface functionalities. Lee *et al.* [36] showed that hydrothermally prepared titanate nanotubes are efficient photocatalysts upon UV-light irradiation. The effects of annealing, sodium content, and crystallinity in the TNTs were also examined. One of the downsides to sodium titanate nanotubes is that the sodium content decreases the photocatalytic efficiency of the materials, due to the sodium hindering the formation of the photoactive anatase phase, however, sodium content increases the nanotubular stability when annealed [36]. Annealing can cause the tubular structure to collapse to rods or even back to particles, but annealing is usually required to obtain anatase phase. A collapse of the nanotubular structure has again a detrimental effect on the surface area of the nanotubes. Therefore, it is a careful balance between the crystallinity, surface area, pore size and sodium content, to obtain an efficient titanate photocatalyst. Hydrothermal TNTs have also been studied under simulated solar light by Guo *et al.* [47]. The TNTs showed outstanding photocatalytic decolorization of RhB and MO when compared to titania nanorods and Degussa P25. The photocatalytic properties of the TNTs were attributed to a large surface area, favorable crystal structure, i.e. anatase, and the oxygen vacancies in the anatase structure contributing to the photocatalytic oxidation process.

Similar to hydrothermal TNTs, TNTs prepared by anodization are widely studied photocatalysts under UV light [49, 51, 54]. However, as titania is a well-known photocatalyst under UV-light due to its properties, more effortsare directed towards modifying the TNT structure in order to reduce the band gap to the visible light range. The band gap needs to be reduced to obtain visible light activity, and similar to $TiO_2$ particles, the electronic properties of TNTs are modified with non-metals [51, 55] or metals [51]. Doping, decoration and composites of $TiO_2$ structures are reviewed in Section 1.1.2.

Nonetheless, TNTs prepared by RBA have not been thoroughly studied as a photocatalyst for organic contaminants yet. The few studies include AO7 [50], MO [49] and MB [56] as model pollutants under UV light only. There are some studies on doped RBA TNTs used as photocatalysts under UV and solar light for hydrogen production [9, 10, 57].

### 1.1.2 Titania based composites

$TiO_2$ mainly absorbs UV light due to the band gaps of the $TiO_2$ structures, such as anatase and rutile. However, UV-light is only a small portion of the sunlight spectrum and to extend the spectral response to the visible light range $TiO_2$ structures are doped with non-metals or metals or coupled with other materials altogether to form composites. The first step towards visible light photocatalysis using $TiO_2$ was commenced by Sato [58] in 1986, when Sato reported nitrogen impurities in $TiO_2$ originating from the use of $NF_4OH$ in the preparation. This $NO_x$ doping of $TiO_2$ shifted the band gap to 434 nm. Presently, N-doped $TiO_2$ structures have been widely studied [59, 60, 61], and even N-doped TNTs are reported [62]. Other non-metals have also been investigated, such as carbon [61], sulfur [61], fluorine [63], iodine [64] and chlorine [65], as well as metals. Metals can be either doped as ions [66] or metal particles [67].

$TiO_2$ composites with noble metals have gained attention as visible light photocatalysts, due to the size and shape dependent plasmon resonance of the noble metals [67]. A semiconductor photocatalyst, such as $TiO_2$, coupled with a noble metal (e.g. Ag) forms a so-called plasmonic photocatalyst. The major processes in a plasmonic photocatalyst are described in Fig. 1.3, where an Ag particle is partially embedded in an n-type $TiO_2$ particle. The major processes in this example include the Ag particle absorbing visible light, whereas the $TiO_2$ particle absorbs UV-light. The visible light formed localized surface plasmon (LSPR) resonance in Ag creates collective oscillations of the electrons, which then create more charge carriers (Fig. 1.3, mark (A)). A space-charge region (Schottky junction) is created when the electrons diffuse from the $TiO_2$ side to the Ag side, leaving behind a positive zone in the $TiO_2$ particle. Fig. 1.3, mark E illustrates the internal electric field in an equilibrium state, where an equal amount of electrons are trapped on the Ag surface as there are positive holes in the space charge region. Mark B in Fig. 1.3 shows a UV-light induced electron-hole pair, however, when this occurs in the space-charge region the electron is forced to the $TiO_2$ and the hole to the Ag particle. The surface confined electrons and holes then participate in redox reactions. Mark (C) illustrates an LSPR generated electron moving across the space charge region to the conduction band of $TiO_2$ [14]. This implicates that the metals provide traps for the photoinduced charge carriers, which reduces electron-hole recombination and increases the visible light absorption efficiency of the noble metal-titania composite. Of the noble metals, silver has received much of the attention, partially due to the lower cost of silver compared to gold and platinum. Silver has been decorated onto $TiO_2$ using various routes, such as photochemical impregnation [68], and sol-gel methods [69].

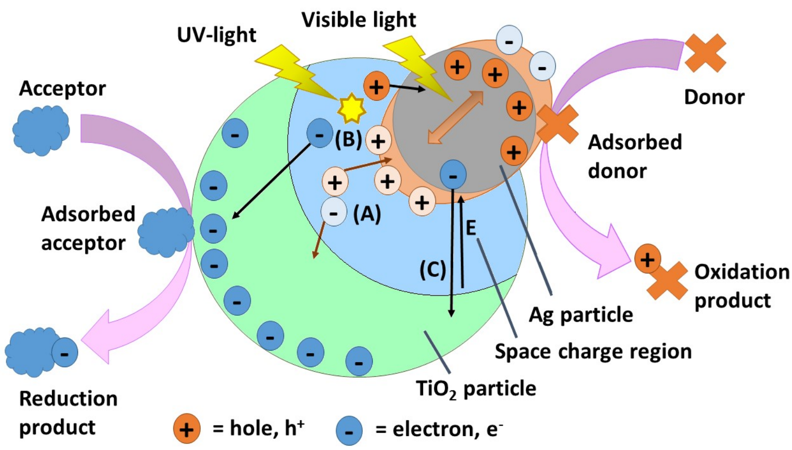


**Figure 1.3.** A schematic representation of the major processes involved in plasmonic photocatalysis. Reproduced after [14].

Carbon-doped titania systems, such as graphene- or graphene derivative-titania systems have also been investigated due to increased charge separation, and the ability to be used as an electron carrier [22, 23, 70, 71, 72, 73]. Graphene is an attractive material to use in a composite due to its unique electronic properties, transparency, flexibility, large surface area and adsorptive properties. Graphene is nowadays a well-studied material consisting of a one atom thick layer of $sp^2$ bonded carbon atoms arranged in a honeycomb lattice [74]. The use of graphene in composites is facilitated by modification of the surface properties, as in the case of graphene oxide (GO). Graphene oxide is the oxidized version of graphene, which can be prepared by oxidation of graphite and separated to single sheets of oxidized graphene layers. GO can be prepared by the well-known Hummers' method [75] or modified versions of it [76]. The graphene-titania composites can be prepared by hydrothermal methods and consist mainly of titania with up to 20 wt. % graphene [77]. The most common and photocatalytically active graphene or graphene derivative loading is below 5 wt.% in the composites [23, 71, 72]. The oxidation degree of graphene oxide modifies the electronic properties and a high oxidation degree may decrease the electronic conductivity, but increase the adsorptive properties. Consequently, it is a careful balance between the oxidation degree and loading of GO in the titania composite, but it also depends on the structure of titania as discussed earlier. As expected, the $TiO_2$-graphene composites are excellent photocatalysts for organic contaminant degradation under UV-light [72] and perform well under visible light as well [23].

These graphene-titania composites can further be functionalized with silver to extend the photocatalytic efficiency even more to the visible light range and to form new composite structures. Only a few reports on graphene, GO or reduced graphene oxide (RGO) together with $TiO_2$ and Ag have been published [78, 79, 80, 81, 82, 83, 84]. The photocatalytic efficiency of these ternary composites, i.e. degree of degradation of the model pollutants, under solar- or visible light irradiation was improved from that of graphene-$TiO_2$ or $TiO_2$-Ag separately. The photocatalytic mechanism is also different from two-component systems, and two suggested mechanisms are represented in Fig. 1.4. The mechanism in Fig. 1.4a is shown for an Ag-GO-$TiO_2$ composite and in Fig. 1.4b for an RGO-$TiO_2$-Ag composite. The mechanism is dependent on the bonding between the components and thus, the graphene or graphene derivative loading and quality affect the photocatalytic efficiency, however, also the positioning of Ag in the composite affects the mechanism. In Fig. 1.4a the composite is irradiated by solar light, of which $TiO_2$ absorbs UV-light. An electron is excited from the valence band to the conduction band in titania, from where the electron is transferred to GO. The electron would then move further to the silver particle. Another option is that the excited dye (dye$^*$) could transfer an electron to $TiO_2$ or GO, due to the dye being adsorbed on the GO, and then further to the Ag particle [80]. Fig 1.4b shows the $TiO_2$, RGO and silver in a different order in the composite and under visible light irradiation. Due to visible light irradiation, silver is the main active photocatalyst generating electrons in Fig 1.4b. The photogenerated electron is proposed to move from silver to the conduction band of $TiO_2$ and further to RGO. RGO is suggested to function as a promoter for electron transport, which leads to a slower recombination of charge carriers and separation of the photogenerated electrons and holes [83].

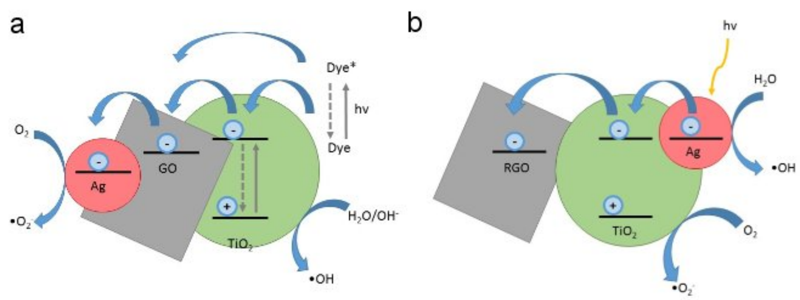


**Figure 1.4.** Schematic representations of the suggested photocatalytic mechanisms of a) an Ag-GO-$TiO_2$ composite and b) an RGO-$TiO_2$-Ag composite. Reproduced according to [80] and [83], respectively.

The photocatalytic mechanism is changed even more when adding other components to the photocatalyst mix. Wang *et al.* [85] studied a Ag-AgBr/$TiO_2$/RGO photocatalyst under visible light. It was hypothesized that the SPR of Ag, visible light active AgBr, the electron transfer of graphene and the $TiO_2$ photocatalyst could arise a synergistic effect to improve the photocatalysis even further. The quaternary composite did outperform all other tested composites, among these Ag/$TiO_2$/RGO, Ag-AgBr/$TiO_2$, Ag/$TiO_2$ and RGO/$TiO_2$. The suggested mechanism is similar to that of Fig. 1.4b, but AgBr can also absorb visible light and participates in the charge carrier formation. The photoinduced electrons in

AgBr are transported to Ag, which hinders Ag from dissolving, and renders the composite more stable. The holes in AgBr oxidizes $Br^-$ to $Br^0$, which then further participates in the redox reactions. AgCl has a similar effect in the visible light active AgCl@Ag/titanate nanotubes/nitrogen-doped reduced graphite oxide composite photocatalyst reported by Pan *et al.* [86], and the suggested mechanism supports the statements of Wang *et al.* [85].

## 1.2 Antibacterial properties of silica and silver materials

This section describes silica as a material and how multifunctional it can be when a composite is formed with silver. Selected preparation processes and properties of silica particles and different silica-silver structures are presented and discussed.

### 1.2.1 Silica

Silica, when looked up in Dictionary.com is defined as "*the dioxide form of silicon, $SiO_2$, occurring especially as quartz sand, flint, and agate: used usually in the form of its prepared white powder chiefly in the manufacture of glass, water glass, ceramics, and abrasives*" [87]. Silica is found in glasses [88], films [88], ceramics [89] and abrasives [90], but it is also used in medical applications, such as in drug delivery [91].

Silica exists in both amorphous and crystalline form. Amorphous silica does not have any specific order in the crystal structure, whereas crystalline silica possesses a systematic structure between the silicon and oxygen atoms. Even though both crystalline and amorphous silica have the same chemical formula of $SiO_2$, the differences in the properties are significant. For example, the health hazards caused by asbestos (a silicate mineral) and silicosis from inhalation of crystalline silica [92] is well known. Amorphous silica, on the other hand, is inert and biocompatible and is thus a good matrix in e.g. drug delivery [93] and antibacterial applications [91].

Amorphous, spherical silica particles can be prepared by the Stöber method [94] or a modified version of it. The Stöber method produces perfectly spherical, monodispersed, nano- to micro-sized, amorphous silica particles. The synthesis procedure is simple and consists of two solvents (water and an alcohol), a silica precursor- often tetraethyl orthosilicate (TEOS), and ammonia as a catalyst. The process involves hydrolysis and condensation reactions producing spherical silica particles. The size of the particles can be modified by the concentration of ammonia added during the synthesis. This synthesis approach can also be used for the formation of other structures, such as core-shell particles [95], with only small modifications to the Stöber method.

### 1.2.2 Antibacterial properties of silver and silica-silver composites

Silver has been known to be antibacterial since ancient times and is still used in medical devices, such as catheters [96]. The interest in silver has increased with the emergence of antibiotic-resistant bacteria, as these bacteria may force us back to a time of non-treatable infections. The antibacterial properties of silver are based on the different forms of silver, i.e., metallic silver, silver ions and silver radicals, and their action on the microbes [97, 98, 99]. The mechanism of the antibacterial action of silver is still under debate, but a few theories persist. The silver cation ($Ag^{+}$) is a soft acid and acids are prone to react with bases. The cell walls of the bacteria are soft bases as they are built up from phosphorous and sulfur, which would lead to damage or destruction of the cell walls. DNA (DNA, deoxyribonucleic acid) also has phosphorous and sulfur constituents with which $Ag^{+}$ can react and destroy. The $Ag^{+}$ interaction with DNA could lead to DNA replication issues and cause microbe termination [100]. $Ag^{+}$ can also react with thiol groups in the bacterial enzymes, which results in their inactivation or destruction [100]. Silver nanoparticles can also release silver radicals, which induce membrane damage [99]. As silver has a diverse antibacterial action mechanism, it is difficult for the bacteria to develop resistance. However, silver nanoparticles have restrictions, as the NPs are prone to agglomeration resulting in larger silver particles, which show a reduced antibacterial efficiency [101].

Silver nanoparticles are usually prepared by solution-phase synthesis, which involves reduction of a silver salt in a solution using, for example, sodium borohydride, ascorbic acid or sodium citrate as reducing agent [102, 103]. Other preparation approaches to make silver structures include: silver reduction in solid matrices by annealing [88], arc-discharge [104], photoreduction of silver ions [105], and electrolysis [106]. All preparation methods have their drawbacks. For example, the silver nanoparticles tend to agglomerate without stabilizers and stabilizer-free methods usually produce a wider size distribution of silver particles and the size control is problematic [103].

Silver nanoparticles have a large surface area and are prone to agglomeration due to the high surface energy [103] and van der Waals forces [107]. Additives or stabilizers, such as polyvinylpyrrolidone (PVP) and sodium citrate [102], are often added to hinder agglomeration of silver nanoparticles. Furthermore, the silver nanoparticle size can be controlled by varying the amounts of reactants in the synthesis. Agnihotri *et al.* [101] used silver nitrate as silver precursor, sodium borohydride as reducing agent and sodium citrate as stabilizer. By varying the concentrations of these reactants silver nanoparticles from 5 nm up to 100 nm are obtained. However, the additives or stabilizers are not always biocompatible and therefore inorganic composites, such as $SiO_2$-Ag are studied.

The main reason for hindering silver nanoparticle agglomeration and thus using stabilizers is that, small silver nanoparticles below 10 nm in size show a higher antibacterial efficiency [101]. Smaller silver particles have a larger surface area as compared to the same concentration of larger particles. For example, when the radius of a spherical particle is doubled the surface area is reduced by half, if the concentration of silver is the same in each case. As the active surface area of smaller particles is larger, the concentration of silver used in antibacterial applications can be reduced to correspond to the surface area of larger particles. This is supported by the findings of Agnihotri *et al.* [101], as a decreasing concentration of silver prevents the bacterial growth when the silver size is reduced.

Amorphous silica is biocompatible and is thus commonly used in different composite structures. Silica-silver ($SiO_2$-Ag) composites have been investigated for other applications, such as for catalytic purposes [108], surface-enhanced Raman spectroscopy (SERS) [109], and in antibacterial applications [110]. The different applications require a variety of forms of $SiO_2$-Ag and as the structures are tunable, many different structures have been investigated, e.g., Ag in $SiO_2$ films [88], Ag in bioactive glass [111], core-shell particles [108], and Ag decorated $SiO_2$ particles [109]. However, in this thesis the focus is on the preparation and properties of $SiO_2$-Ag structures used for antibacterial applications. When using silver in antibacterial applications, it is highly desired that the silver would have a prolonged antibacterial effect. This requires immobilization of silver and a sustained release of silver species to the intended location.

The immobilization of silver is often achieved by forming a silica shell on the silver nanoparticle, which then forms a core-shell particle. The silver nanoparticles are prepared first by a method described above, i.e., solution-phase synthesis, followed by silica shell formation [112]. However, to obtain a controlled release of silver from the silica-silver composite a porous structure is usually preferred. A porous structure in the silica shell is obtained by using a template, such as hexadecyltrimethylammonium bromide (CTAB) [91, 113]. Immobilization of silver can also be achieved by fixing the silver on the surface of silica, i.e., decorating silica with silver. This can be done by multi-step processes by first preparing the silica particles and then functionalizing the surface with polymers [103] or silanes [114], followed by addition of the silver precursor and finally reducing the silver ions to silver.

When considering antibacterial activity, it has been shown that silver is more efficient against Gram-negative bacteria, for example, *Escherichia coli* (*E. coli*) [99, 115]. However, antibacterial activity against Gram-positive bacteria is also important, specifically since the antibiotic-resistant Methicillin-resistant *Staphylococcus aureus* (MRSA) is of Gram-positive type and common in wounds [116]. When considering using the silica-silver composites for antibacterial purposes the specifications of the applications should be considered, for example, a sustained release is preferred in applications for wounds. This means that the immobilized silver has to be released over longer periods of time in sufficient concentrations to hinder bacterial growth. To obtain the aspired sustained release of silver species the composite structure needs to be optimized and the release conditions investigated.

## 1.3 Aim of the research

This thesis focuses on means to counteract harmful organic pollutants and bacteria in our surroundings. The approach is to develop titania and silica-silver based nanomaterials. The titania based nanomaterials are developed as high efficiency photocatalysts for organic contaminant removal and the silver-containing composites for antibacterial purposes. The work focuses on the preparation of the materials and how the properties are affected by the processing parameters.

Novel titania photocatalysts can be achieved in two ways: by developing a different morphology or coupling titania with other materials. This thesis focuses on tuning the morphology of titania nanotubes by optimizing the nanotube processing conditions, as well as, preparing a quaternary titania composite coupled with other materials to enhance the photocatalytic efficiency.

*The morphological properties of the nanotubes and the composites are examined by identifying the crystalline phases, size and shape related properties, and surface functionalities. The photocatalytic efficiency is measured through model dye decolorization for a period of 3 h under either UV-light or natural sunlight irradiation.*

Antibacterial properties of silver containing composites are dependent on size and shape of the silver nanoparticles. The growth of an optimal silver nanoparticle size in a silicon dioxide particle matrix is investigated. The composite is also subjected to dissolution tests to examine the release rate of silver from the composite to verify a sufficient silver concentration for a prolonged antibacterial effect. A suitable silica-silver candidate is then chosen for antibacterial studies in powder form and incorporated in wound dressings.

*The growth of the silver nanoparticle size is examined by heat treatment and the sizes are measured from electron microscope images. The dissolution tests are performed at different temperatures and pH to obtain a perception of the dissolution affecting variables. The antibacterial tests using the composite probe the efficiency of the composite by hindering the growth of bacteria in vitro. The optimal loading of composite for a prolonged release is studied before incorporation in wound dressings.*

# 2. Materials and methods

This chapter describes the preparation of the nanomaterials and composites, and the characterization methods used for evaluating the materials properties. The details are found in the publications attached to this thesis.

## 2.1 Preparation of the materials

This section introduces the different material preparation methods used in this thesis.

### 2.1.1 Preparation of titanate and titania nanotubes

**Sol-gel synthesis of titania** Titania was prepared by a sol-gel method previously developed in our lab [117]. The titania was formed by mixing $Ti(OBu)_4$ ($\geq$ 97 %, Sigma-Aldrich) and 1-butanol (>99 %, Sigma-Aldrich) for 5 min and then slowly adding 0.5 mL concentrated HCl (37 %, ACS). HCl was used as a catalyst to start the hydrolysis reaction. The solution was left to react for 2 h under magnetic stirring, followed by ageing and drying. The resulting titania was heat treated at 400 °C for 3 h to obtain anatase structure and to remove carbonaceous impurities.

**Chemical processing of titanate nanotubes** The titanate nanotubes were prepared by a chemical processing method introduced by Kasuga *et al.* [25]. The anatase titania powder prepared as described earlier was used as titania source for the titanate nanotubes. The titania powder was reflux heated in 10 M NaOH (from NaOH pellets, $\geq$ 98 %, Sigma-Aldrich) solution at 110 °C for 21 h. During this process, titania sheets were formed. The mixture was subsequently washed and centrifuged with de-ionized water until a conductivity of 70 $\mu$Scm$^{-1}$ was reached. The titanate nanotubes were then treated with 0.1 M HCl solution for 2 h, followed by washing with water until the conductivity was less than 10 $\mu$Scm$^{-1}$. The titanate sheets roll up to form tubes during the washing process. The powder was dried at 60 °C for 12 h, followed by heat treatment at 300-700 °C for 3 h to examine change in the crystal structure. Further details are found in Publication I.

**Preparation of titania nanotubes using rapid breakdown anodization** The titania nanotubes (TNTs) powders were prepared by rapid breakdown anodization. In brief, a conventional two-electrode setup was used; 0.25 mm thick titanium foil (99.7 %, Sigma-Aldrich) cut into 12 x 12 mm pieces were used as the anode, 0.1 M perchloric acid (diluted from 70 % $HClO_4$, Sigma-Aldrich) as the electrolyte, and Pt foil as the cathode. The distance between the electrodes was kept constant at 10 mm. The anodization was conducted at 20 V. The TNT powder began forming immediately and was collected from the electrolyte by centrifugation when the Ti foil was fully converted into TNT powder. The TNT powders were washed with DI-water and dried at 60 °C. The TNT powders were then annealed at 250 °C, 350, °C, 450 °C, and 550 °C. The powders were named according to the annealing temperatures, e.g. "TNT-250" was annealed at 250 °C. Further details are found in Publication II and [18].

**Preparation of electrodes** The electrodes used in the photocurrent and electrochemical impedance spectroscopy measurements were prepared by depositing a film made of RBA TNTs on fluorine-doped tin oxide (FTO) glass. The films were drop cased on the FTO glass using a suspension prepared from TNT powders in ethanol. The films were dried at 70 °C for 20 min in air, followed by adhering the films to the FTO glass with Nafion (Sigma Aldrich; 5 wt. % in lower aliphatic alcohols and water) and then dried again at 70 °C for 20 min in air.

### 2.1.2 Synthesis of silica-silver composite

The synthesis of the silica-silver composite powder was based on a modified Stöber method [118]. Ethanol (96.1 vol.%, Altia), $NH_4OH$ (25 % JT Baker), $AgNO_3$ (≥ 99.0 %, Sigma-Aldrich) and de-ionized water were mixed by magnetic stirring until the $AgNO_3$ was dissolved. Tetraethyl orthosilicate (TEOS, ≥ 99.0 %, Sigma-Aldrich) was added to the solution dropwise for silica formation. The solution was left to react for 2 h and during this time a white precipitate formed. The $NH_4OH$ has two functions: i) it participates in the formation of $[Ag(NH_3)_2]OH$ complex and ii) serves as a catalyst for silica formation. The precipitate was collected by centrifugation and dried at room temperature. The dried product was further heat treated at 300-800 °C for 75 minutes to observe silver particle growth. The full synthesis is described in Publication IV.

### 2.1.3 Synthesis of graphene oxide-titania-silver-silver chloride composites

The preparation of the graphene oxide-titania-silver-silver chloride composites was divided into four parts. Graphite oxide and titania were prepared separately, with the exception when using commercial Degussa P25 titania. The in-house made titania was prepared by the method described in 2.1.1, in other cases commercial Degussa P25 titania was used. Details of the synthesis are found in

Publication III.

**Preparation of graphite oxide** Graphite oxide was prepared by a modified Hummers' method [75, 76]. The synthetic graphite was pre-oxidized using phosphorous pentoxide ($P_2O_5$, ≥ 98.0 %, Sigma-Aldrich) and potassium persulfate (≥ 99.5 %, Sigma-Aldrich) in concentrated sulfuric acid (95-97 %, Sigma-Aldrich) under constant stirring at 80 °C for 4 h. The dispersion was diluted with 1000 mL de-ionized water, centrifuged and washed repeatedly until pH 5 was reached. The obtained powder was then dried in vacuum at 40 °C. This pre-oxidized graphite was then dispersed in concentrated sulfuric acid. Potassium permanganate (≥ 99.0 %, Sigma-Aldrich) was carefully added while keeping the temperature below 10 °C to further oxidize the pre-oxidized graphite. The temperature was elevated to 35 °C when the final addition of potassium permanganate was completed. Some water was added after 2 h and the reaction terminated by addition of hydrogen peroxide (30 %, Sigma-Aldrich). The graphite oxide was then washed repeatedly with water until pH 5, followed by drying in vacuum at 50 °C and ground to obtain a fine powder.

**Decoration of titania with silver and silver chloride** Titania, either in-house made or commercial Degussa P25 (≥ 99.5 %, Aeroxide), was decorated with silver and silver chloride by adding an aqueous solution of silver nitrate to a dispersion of titania, ammonium hydroxide, and ethanol. A polyvinylpyrrolidone (PVP, MW ≈ 10 000, Sigma-Aldrich) stock solution was prepared by dissolving 25 g PVP in 50 mL water. PVP was investigated as a reducing agent in two concentrations, namely 2.5 mL or 5.0 mL PVP stock solution in 100 mL ethanol. AgCl was formed by adding HCl to the mixture. The obtained product was centrifuged, washed and dried at 50 °C.

**Preparation of graphene oxide-titania-silver-silver chloride composite** The graphene oxide-titania-silver-silver chloride composites were prepared with 50 nominal weight percent graphite oxide and 50 nominal weight percent titania-silver-silver chloride. The powder mixtures were added to 50 mL water and sonicated for 60 minutes in order to exfoliate graphite oxide to graphene oxide and to form a homogeneous composite. The abbreviations for the composites are GOTAAC-2.5, GOTAAC-5, GOPAAC-2.5, GOPAAC-5. GO is graphene oxide, P is for commercial Degussa P25 titania and T for the in-house made titania, A stands for Ag, and AC for AgCl. The numbers stand for how much PVP was added during the synthesis.

## 2.2 Characterization

### 2.2.1 Phase and crystal structure

The phase and crystal structure of the powders were determined using X-ray diffraction (XRD). The measurements were carried out on a PANalytical X'Pert

Powder Pro diffractometer using Cu $\kappa_{\alpha_{1/2}}$ radiation having $\lambda_{\alpha_1}$ = 1.54060 Å at the voltage of 45 kV and 40 mA current or Co $\kappa_\alpha$ radiation having $\lambda$ = 1.790 Å at a voltage of 40 kV and 40 mA current in a chosen $2\theta$ range. The XRD patterns were analyzed using HighScore Plus software equipped with the International Centre for Diffraction Data (ICDD) database. Rietveld refinement of different phases was carried out using Powdercell 2.4.

### 2.2.2 Morphology

Surface morphology and particle sizes were analyzed using Scanning Electron Microscopy (SEM). SEM was performed with a Hitachi S-4700 cold Field Emission Gun Scanning Electron Microscope (FEG-SEM). X-ray energy dispersive spectrometry (EDX) analyses were carried out by Tescan Mira3 FEG–SEM equipped with a Thermo Scientific NSS spectral imaging system for elemental analysis.

Particle sizes, morphology, and the crystalline structure were characterized by Transmission Electron Microscopy (TEM) using a Tecnai F20 G2 200 kV FEG Transmission Electron Microscope operating at 200 kV.

### 2.2.3 Chemical composition

The functional groups in the studied powders were determined using Fourier Transform Infrared (FTIR) spectroscopy using a Nicolet 380 FT-IR. Most measurements were carried out in attenuated total reflectance (ATR) mode in the spectral range of 525-4000 $cm^{-1}$. The samples in Publication I were prepared using the KBr method, in which 1 % TNT powder was mixed with dried KBr and pressed to pellets prior to measurement.

The surface chemical composition of selected powders was analyzed with X-ray Photoelectron Spectroscopy (XPS). The measurements were realized by using AXIS Ultra electron spectrometer by Kratos Analytical at 285.0 eV as the charge was referenced to adventitious C1s peak.

Structural investigations were made with Raman spectroscopy. The Raman spectra were recorded using Labram HR Raman Spectrometer (Horiba Jobin-Yvon) with Argon laser excitement of 514 nm at 10 mW equipped with a 50x BX41 objective by Olympus. The peak values were determined with either Gaussian or Lorentzian peak fits.

### 2.2.4 Optical studies

A Hitachi U-5100 UV-vis spectrophotometer was used to record the surface plasmon resonance (SPR) peaks and the absorption of solutions. The UV-vis diffuse reflectance spectra (DRS) were determined using UV-Vis-NIR Perkin Elmer Lambda 950 or UV-Vis-NIR Agilent Cary 500 equipment with an integrating sphere. The measurements were calibrated with a Spectralon disc. The band gaps were obtained from the absorbance edge wavelengths by using the equation:

$$E = \frac{hc}{\lambda} \tag{2.1}$$

Photoluminescence spectroscopy (PL) was used to examine the photogenerated electrons. The PL measurement was carried out using a Perkin Elmer LS 50B Luminescence spectrometer equipped with a 20 W Xenon lamp using an excitation wavelength of 330 nm.

The photocurrent measurements were performed on a Jaissle IMP83 PC-T-BC potentiostat at 500 mV. A three-electrode setup with Pt as a counter electrode, the TNT film deposited on FTO glass as a working electrode and an Ag/AgCl reference electrode was used. The measurement was performed in a 0.1 M $Na_2SO_4$ (Sigma-Aldrich; ≥ 99.0 %) solution and the sample irradiated in the range of 250-600 nm using an Oriel 6365 150 W Xenon lamp connected to an Oriel Cornerstone 130 1/8 m monochromator.

### 2.2.5 Thermal behavior

Thermogravimetric analysis (TGA) was carried out using a Perkin Elmer TGA7 device in $N_2$ atmosphere in the range of 31 °C to 800 °C at a heating rate of 10 $°\mathrm{Cmin}^{-1}$ to observe any thermal decomposition of the samples.

### 2.2.6 Electrochemical studies

A Gamry Reference 600+ potentiostat by Gamry instruments was used for electrochemical impedance spectroscopy (EIS) studies. A three-electrode setup with Pt as a counter electrode, the TNT film deposited on FTO glass as a working electrode and an Ag/AgCl reference electrode (+ 0.199 V vs RHE, Radiometer Analytical) was used. The electron transfer was studied using an outer sphere redox probe (5 mM $Ru(NH_3)_6^{2+/3+}$ in 1 M KCl). The EIS measurement was performed from 200 kHz to 100 mHz using an AC signal of 15 mV.

### 2.2.7 Specific surface area and porosity

Specific surface area (SSA) and pore size distribution were determined by $N_2$ adsorption-desorption measurements at 77 K using a Tristar II 3020 device. The samples were dried and degassed prior to carrying out the measurements. Brunauer-Emmet-Teller (BET) analysis was used for specific surface area and Barrett-Joyner-Holenda (BJH) adsorption isotherms were used for porosity assessment. A Bel Belmaster Mini II device was also used in PIV.

### 2.2.8 Dissolution of silver

The concentration of Ag from the dissolution tests was measured using Inductively Coupled Plasma Atomic Emission Spectroscopy (ICP-AES) and carried out on a Perkin Elmer ICP-AES Optima 7100 DV. The silver emission spectrum was probed at 328.068 nm and 338.289 nm. The error of the measurements was estimated as ± 5 %.

### 2.2.9 Photocatalytic experiments

The photocatalytic experiments were realized by measuring the decolorization of model pollutants, i.e. methylene blue (MB), methyl orange (MO) or Rhodamine B (RhB). The decolorization under UV light was carried out in an in-house built device equipped with two Philips PL-S 11W/102P UV lamps emitting UV radiation in the range of 350-400 nm with the irradiance of 1 $mWcm^{-1}$. The natural sunlight tests were performed under natural sunlight in Espoo, Finland (60°11'01.3"N 24°49'32.2"E)) during June-July 2017. The loading of the photocatalyst was 30 mg (PIII), 50 mg (PI), and 100 mg (PII). Reference $TiO_2$ powders were used for comparison, i.e., Degussa P25 $TiO_2$ (anatase-rutile mixture, Aeroxide, ≥ 99.5%, Sigma-Aldrich) in PIII, commercial anatase $TiO_2$ (anatase, Sigma-Aldrich, 99.8 %) in PII and in-house made $TiO_2$ (anatase, as prepared in section 2.1.1) in PI. All photocatalysts were dispersed in 100 ml of aqueous model pollutant of the concentration 10 $mgL^{-1}$ (PI, PII) or 30-40 $mgL^{-1}$ (PIII). The photocatalyst dispersions were left under dark conditions to reach adsorption-desorption equilibrium prior to irradiation. The adsorption-desorption equilibrium was considered reached when the concentration of the solution was unchanged. The adsorption capacity ($Q_e$) is expressed as:

$$Q_e = \frac{(C_a - C_e)V}{m}, \tag{2.2}$$

where $C_a$ ($mgL^{-1}$) is the initial concentration of the model pollutant and $C_e$ ($mgL^{-1}$) is the concentration when adsorption-desorption equilibrium is reached. V (L) is the volume of solution at equilibrium and m (g) the mass of the photocatalyst/adsorbent.

The concentration of the dye solutions after equilibrium was measured and defined as the initial concentration ($C_0$). The concentration (C) was measured for samples that were withdrawn in 3 ml aliquots at given time intervals and filtered through 0.45 $\mu$m Nylon syringe filters or centrifuged to remove any catalyst particles. The change in concentration ($C/C_0$) is proportional to the variation in absorbance ($A/A_0$), where A is the measured absorbance at time t and $A_0$ the initial absorbance after dark adsorption. The filtrates were analyzed by observing the change at the maximum absorbance peak of the dye, i.e. MB $\lambda_{max}$ = 664 nm, MO $\lambda_{max}$ = 465 nm, and RhB $\lambda_{max}$ = 554 nm using UV-vis spectrophotometry.

### 2.2.10 Antibacterial experiments

The antibacterial efficiency of the $SiO_2$-Ag 300 composite was studied for antibacterial wound dressing applications using Gram-positive Methicillin-Resistant *Staphylococcus aureus* (MRSA, ATCC 43300, KWIC-STIK, Microbiologics) and Gram-negative *Escherichia coli* (E. coli, VTT E-94564) bacteria. Both bacteria were cultured on Luria-Bertani (LB, BD Difco) agar overnight at 37 °C for the antibacterial tests.

Two disinfection methods were investigated for the $SiO_2$-Ag 300 composite powder, i.e., UV- and filtration sterilization. In UV-sterilization, the powder was irradiated by UV for 12 h before preparing a suspension of sterile Milli-Q water and composite powder. The filter sterilization was carried out by filtering the composite powder through a 0.2 $\mu$m cellulose acetate filter (VWR International). The antibacterial tests were performed under aerobic conditions.

The agar diffusion assays were prepared in duplicates by placing 100 $\mu$L of the bacterial suspensions consisting of ~1-2x$10^8$ colony forming units (CFU)/mL on Mueller-Hinton agar (MHA, Lab M Limited) plates before adding 100 $\mu$L of the previously prepared composite suspension. The inhibition zones (IZs) were measured after overnight incubation at 37 °C.

The $Ag-SiO_2$ composite impregnated wound dressing was prepared by soaking a sterile gauze (~1 cm x 1 cm piece, Mepore, Mölnlycke Health Care) in the composite suspension (1 mg/mL) for 15 minutes. The composite impregnated gauzes ($Ag-SiO_2$-G) were compared to a commercial Ag-containing dressing (CSD, Hansaplast, Beiersdorf AG) and a control gauze (Mepore). The CSD and control gauze were soaked in sterile Milli-Q water. All samples were then placed on MHA plates to inhibit bacterial growth. The tests were prepared in duplicates and the results were measured after overnight incubation. The antibacterial mechanisms of the $SiO_2$-Ag composite on MRSA were studied using TEM for morphological changes.

The minimum inhibitory concentration (MIC) of the $SiO_2$-Ag composite was determined by applying the standard broth microdilution method. The $SiO_2$-Ag composite suspension was diluted from 1 mg/mL to 31.25 $\mu$g/mL in Mueller-Hinton broth (MHB, Lab M Limited). Each concentration was inoculated with bacterial suspensions and the MIC was examined after overnight incubation at 37 °C.

The prolonged antibacterial effect was examined for 3 days. In brief, $Ag-SiO_2$-G, CSD, and control gauze were examined in a test tube containing sterile Milli-Q water, MHB, and MHB-bacterial suspension followed by incubation at 37 °C with shaking. Test tubes without dressings and MHB were used as negative controls and MHB-bacterial suspension as positive control. The samples were inspected every 24 h.

# 3. Results and discussion

## 3.1 Properties of $TiO_2$ and its composites

In this section different $TiO_2$-based structures are described and their pertinent properties are presented and discussed. The focus is on the structures and morphologies of the materials, and their adsorptive and the photocatalytic properties.

### 3.1.1 Morphology and structure

The chemical processing method, which is used for preparing nanotubes, usually yields some kind of nanotubular titanate structure, such as $H_2Ti_3O_7$ [30], $Na_2H_2Ti_2O_4(OH)_2$ [119] and $Na_xH_{2-x}Ti_2O_5 \cdot H_2O$ [33]. The exact crystal structure depends on the used washing conditions [36], i.e. on the amount of sodium remaining from the solvent. The crystalline structure of the present nanotubes was investigated in detail using XRD in Fig. 3.1a. The diffraction curves in Fig. 3.1a reveal a mixed titanate and anatase structure for the as-synthesised nanotubes. The titanate structure matches with $H_2Ti_3O_7$. However, since sodium is present from the washing step the structure is more likely $Na_xH_{2-x}Ti_3O_7 \cdot nH_2O$. The morphological and crystal structure change was examined by annealing the nanotube sample from 200 °C to 700 °C, and it was observed that the anatase structure becomes more prominent when increasing the annealing temperature. However, the titanate structure is observed up to 500 °C, after which it transforms into disodium hexatitanate ($Na_2Ti_6O_{13}$) structure. The crystal structure for the as-prepared nanotubes, i.e., the mixture of anatase and $Na_xH_{2-x}Ti_3O_7 \cdot nH_2O$ has not been reported before (PI). The as-prepared TNT powder prepared by RBA consisted of anatase phase, as shown in Fig. 3.1b. The TNTs formed a mixed phase of anatase and brookite at 450 °C, which further transformed into a mixture of anatase and rutile at 550 °C.

The TEM images in Fig. 3.2 verify the formation of nanotubular structure. Figs. 3.2a and b show the appearace of the nanotubes prepared by chemical

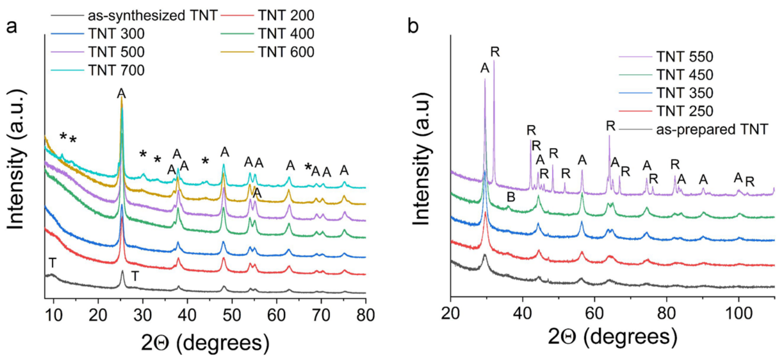


**Figure 3.1.** X-ray diffraction of a) titanate nanotubes prepared by chemical processing and b) titania nanotubes prepared by rapid breakdown anodization. A marks anatase, R rutile, B brookite, * sodium hexatitanate ($Na_2Ti_6O_{13}$), and T $H_2Ti_3O_7$. Modified from Publication I and Publication II.

processing after annealing. The nanotubes are from 60 nm to hundreds of nanometers long, with the outer diameter of 8-10 nm and both ends of the tubes are open. The thermal stability of the tubes was studied by annealing the tubes from 200 to 700 °C for 3 h. The tubes persisted for temperatures up to 450 °C, above which the tubular structure began to transform into rods. At 600 °C all nanotubes were converted into nanorods. The nanotubes prepared by RBA are open in one end and closed in the other end. The nanotubes are in the length of 18 $\mu$m to 35 $\mu$m with pores in the range of 11 nm to 18 nm. When comparing the two preparation methods, a significant change in the thermal stability of the nanotubes was observed. The tubular structure was only retained up to 250 °C for the RBA TNTs, and at 350 °C they were transformed into rods and particles and at even higher annealing temperatures the rods formed into particles, which is shown in Figs. 3.2c and d. The chemical processed tubes retained the tubular structure until 450 °C, which is much higher than for the RBA tubes. The structural and morphological differences are significant and it has been shown that titanate nanotube structures withstand higher temperatures [120, 121], compared to titania nanotubes.

The band gaps for the nanotubes were calculated from diffuse reflectance UV-vis spectroscopy (DRS) measurements. The band gaps reduced slightly from 3.13 eV to 3.06 eV when the titanate nanotubes were annealed. For the RBA TNTs the band gaps remained at 3.1 eV, but at 550 °C the band gap narrowed to 3.0 eV. Band gap shifts are usually due to some change in crystal structure or morphology. The reported values for rutile, brookite and anatase are 3.00 eV [7], 3.1-3.4 eV [13] and 3.23 eV [7], respectively. The reduction in the band gap, as compared to anatase, would indicate that the nanotubes could form electron-hole pairs also under visible light (400 nm ≈ 3.1 eV).

The GO/$TiO_2$/Ag/AgCl composite structures were analyzed by XRD to identify the phases of $TiO_2$, the exfoliation of graphite oxide (GrO) to GO and to verify

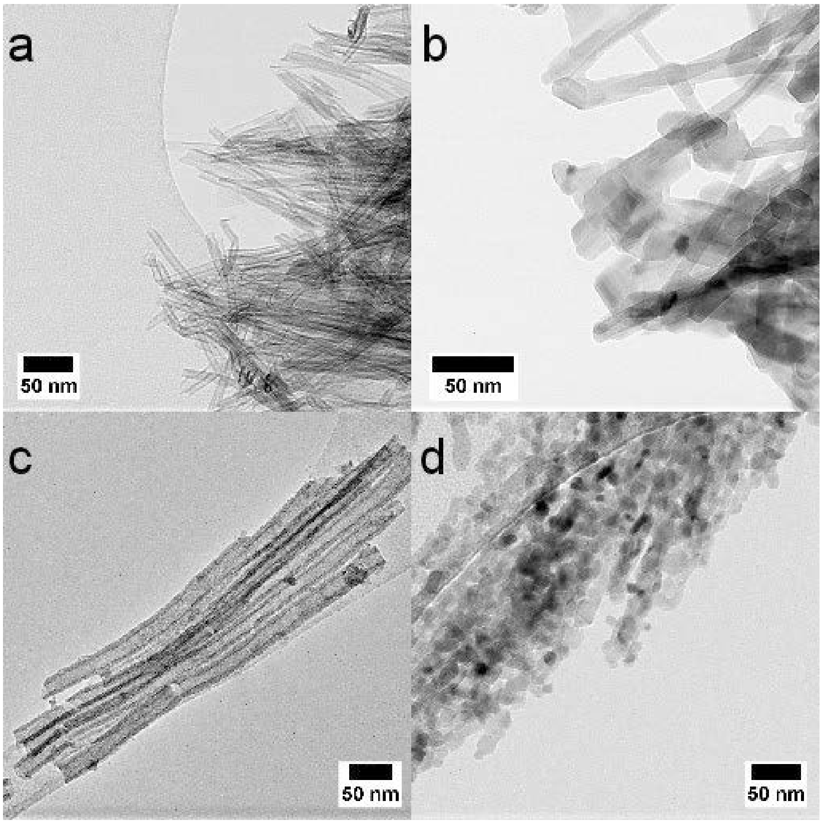


**Figure 3.2.** TEM images of a) the as-synthesized nanotubes prepared by chemical processing and b) the transformation into rods after annealing at 600 °C, c) the as-prepared nanotubes prepared by rapid breakdown anodization and d) the structural change to particles at 350 °C.

the presence of Ag and AgCl. The GrO was not completely exfoliated according to the XRD patterns, as the diffraction peak of GrO 002 plane was still visible. This could possibly be circumvented by longer sonication and grinding times for the GrO. According to Rietveld refinement, the composites containing commercial Degussa P25 $TiO_2$ had a higher weight fraction of rutile and AgCl, as compared to the composites with in-house made $TiO_2$. The XRD analysis did not reveal diffraction from any Ag planes, which should be present due to the reduction of $Ag^+$ by PVP during the synthesis. TEM imaging was performed to see the exfoliation of GrO to GO and the distribution of $TiO_2$ on the GO sheets. As shown in Fig 3.3a, $TiO_2$/Ag/AgCl particles are positioned on a single or few-layer sheet of GO. HRTEM was used to confirm the existence of pure Ag in the composites, as shown in Fig. 3.3b.

The surface area was measured, as the pollutants adsorb on the surface of the photocatalytic material to receive charge carriers, which results in the decomposition of the pollutant. For the titanate nanotubes (PI), the specific

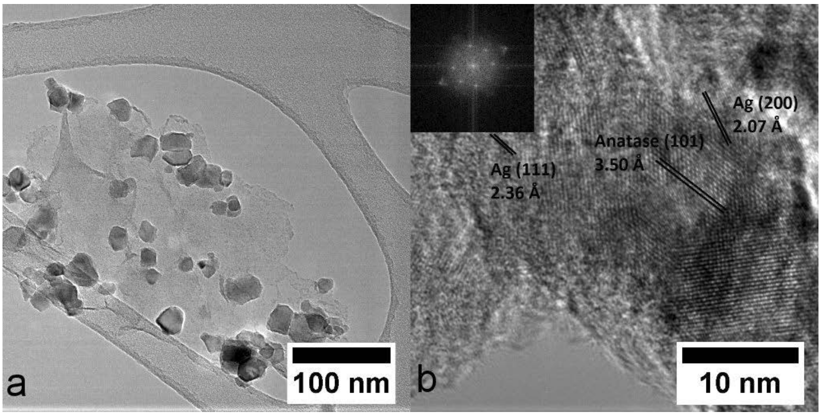


**Figure 3.3.** TEM image of a) GOTAAC-5 sample and b) HRTEM image of GOTAAC-5 showing the interplanar distances of silver. The inset in b) is the Fast Fourier Transform (FFT) pattern of the image. Modified from Publication III.

surface area increased drastically from 61.5 $m^2g^{-1}$ up to 157.1 $m^2g^{-1}$ when the in-house made $TiO_2$ particles converted into nanotubes during the synthesis. For the RBA TNTs, the largest specific surface area was measured for the as-prepared RBA nanotubes (179.2 $m^2g^{-1}$) (PII). However, the surface area decreased when the tubular structure was transformed into rods. The specific surface area for the dry GO/$TiO_2$/Ag/AgCl composite powders (PIII) was in the range of 23-36.9 $m^2g^{-1}$, which is smaller than the surface area for the $TiO_2$ used as precursor. This was probably due to insufficient exfoliation of GO and agglomeration of $TiO_2$/Ag/AgCl-component.

FTIR was measured to obtain information on the functional groups on the materials. Functional groups, especially hydroxide groups (-OH), aid adsorption and photocatalysis reactions by offering the model pollutants places to adsorb on the surface for further decomposition reactions. The FTIR graphs revealing the functionalities of the titania based materials are shown in Fig. 3.4. The nanotubes have hydroxide groups on the surface, but the amount was reduced upon increasing the annealing temperature. The GO/$TiO_2$/Ag/AgCl composites also display hydroxide groups, due to the abundance of -OH groups in GO. Further, the commercial Degussa P25 $TiO_2$ also have hydroxide functional groups whereas the in-house made $TiO_2$ does not (PI).

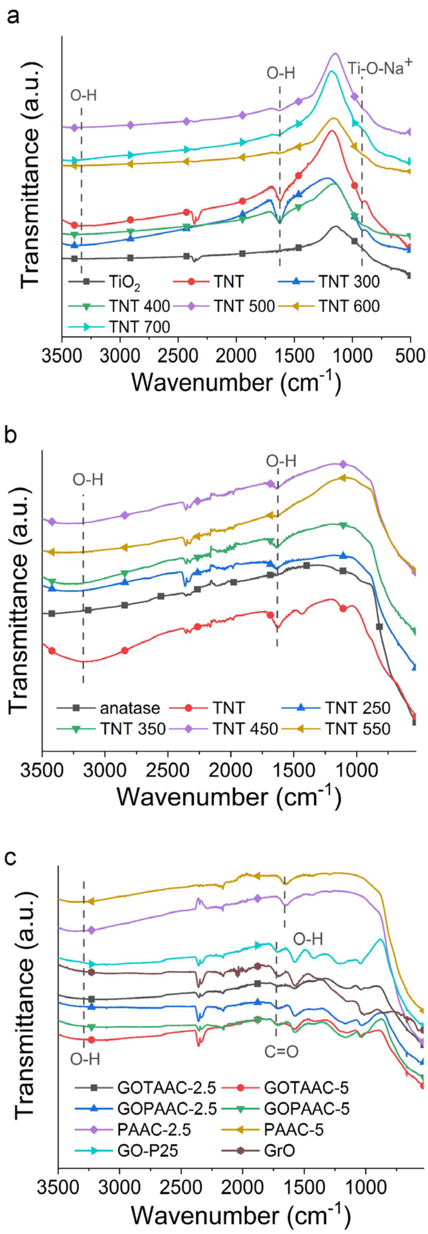


**Figure 3.4.** FTIR of a) the titanate nanotubes, b) RBA nanotubes, and c) the GO/$TiO_2$/Ag/AgCl composites. Modified from PI, PII, and PIII, respectively.

### 3.1.2 Adsorption

The adsorption capability of GO depends on the degree of oxidation [122]. Thus, the adsorption capability of MB onto the GO containing composites was investigated to be able to tune the initial concentration of MB before adsorption to attain an invariable concentration of approximately 10 $mgL^{-1}$ MB at the start of the photocatalytic tests. This procedure enabled to differentiate which composite was a more efficient photocatalyst as the concentration of MB was approximately the same for all experiments. It was also of interest to attain the maximum adsorbance for both pristine GO and for its composites and how the large adsorbance of MB affected the efficiency of the photocatalytically active $TiO_2$/Ag/AgCl-part in the composites.

The degree of oxidation of GO and the initial concentration of MB affected the adsorbance of MB onto the GO surface [122, 123], so the adsorption investigation commenced by studying the adsorption of MB onto GO. The loading of GO was kept constant at 20 mg so that it was possible to make the assumption that the surface area, i.e., active adsorption sites of the powder was kept constant. The adsorption was shown to decrease when increasing the MB concentration (Fig. 3.5a). It is shown in Fig. 3.5b that the GO containing composites adsorb a large quantity of MB. The largest adsorption ($Q_e$) of 98.4 to 112.7 $mgg^{-1}$ was obtained for the GO containing composites. The differences in adsorption may be due to different exfoliation from GrO to GO, assuming the same oxidation degree of the GO.

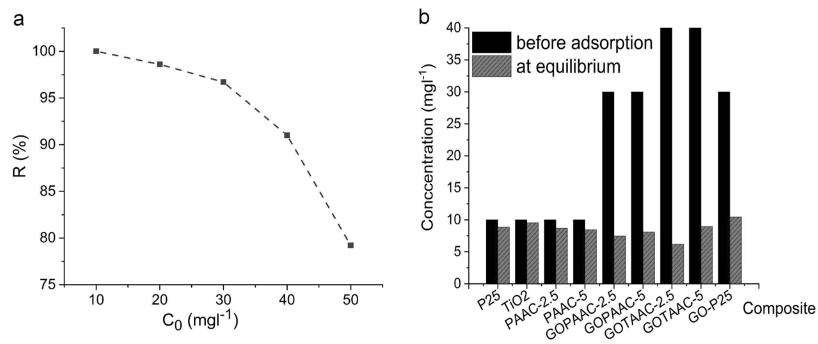


**Figure 3.5.** a) The removal efficiency of MB (R %) for GO (loading 20 mg) when compared to the initial MB concentration. b) The comparison between the initial concentration and the concentration of MB after reaching adsortpion-desorption equilibrium on the studied composite powders. Adapted from Publication III.

### 3.1.3 Photocatalytic activity

The key properties affecting the photocataytic efficiency in photocatalysts were restricted to active surface area, surface functional groups, fast charge carrier recombination, and the band gap, which generate the charge carriers. The developed $TiO_2$ materials in this thesis attempt to improve these properties and the photocatalytic activity was evaluated through decolorization of MB under UV-light irradiation (PI,PIII), and MO and RhB (PII). In addition, decolorization of MO and RhB was also evaluated under natural sunlight (PII).

The decolorization of MB was investigated under UV-light irradiation using the different titanate nanotubes and the in-house made titania as reference material. Fig. 3.6a shows that all synthesized titanate structures displayed photocatalytic activity by decolorizing MB upon UV-light irradiation, however, the in-house made titania showed negligible decolorization. The as-synthesized TNT sample displayed the highest removal efficiency (91 %), followed by TNT 300 (88 %). A general trend was observed for the titanate samples, i.e. the removal efficiency of MB decreased with higher annealing temperatures. The decreasing trend of photocatalytic removal efficiency was attributed partially to the reduction in specific surface area, but also to the decreasing amount of active surface sites, that is hydroxyl groups. The surface area could not be the only factor affecting the photocatalytic activity, since the surface area of the in-house made titania was larger than the surface area of the samples annealed at 500 to 700 °C. The relative amounts of hydroxyl groups also decreased upon annealing the samples, as shown in the FTIR graph in Fig 3.4a. The hydroxyl groups facilitate the adsorption of the cationic MB dye on the surface of the photocatalyst and take an important role in the advanced oxidation reactions required for decolorization [124]. The decolorization can only be negligible without hydroxyl groups due to insufficient adsorption sites, as in the case of the in-house made titania powder. Other structural components also affect the photocatalytic properties, such as crystallinity and band gap. Since all the titanate nanotube powders were prepared under the same conditions it was assumed that the sodium content was constant in all samples, and would thus not cause significant changes in the photocatalytic activity between the samples. The band gaps were also only slightly reduced from 3.13 eV to 3.06 eV. This band gap change is dependent on the analysis of the diffuse reflectance measurement (PI, Fig. 7). The crystal structure change did not reveal significant changes in the photocatalytic activity either, and therefore it was concluded that the photocatalytic activity, in this case, was directly related to the number of reactive sites (-OH groups) in the materials.

Several reports on the decolorization of MB using titanate nanotubes under UV-light irradiation have been published after the publication of Publication I. For example, Sandoval *et al.* [125] reported complete decolorization within 120 minutes of UV light irradiation when using hydrothermally prepared titanate nanotubes, which consisted of different ratios of $Na_2Ti_3O_7$ and $H_2Ti_3O_7$. The nanotubes displayed large adsorption of the MB dye prior to degradation. The nanotubes with lower sodium content had a lower adsorption capability of MB and a higher decolorization and mineralization of MB, due to the favorable band gap (3.15 eV) and the ability to generate sufficient amounts of hydroxyl radicals (OH·). Nanotubes with $Na_2Ti_3O_7$, $H_2Ti_3O_7$, $H_2Ti_4O_9 \cdot nH_2O$ and anatase crystal structures or mixtures thereof, have also been prepared hydrothermally [126, 127, 128]. The maximum decolorization of 90 % was obtained with a combination of adsorption and decolorization of MB under UV-light [127] and reaction rate of 0.0116 $min^{-1}$ [126]. A 90 % removal is close to the maximum removal obtained for TNT (91 %) herein and with the reaction rate of 0.013 $min^{-1}$ (0.78 $h^{-1}$). The TNT mixed structure of $Na_xH_{2-x}Ti_3O_7 \cdot nH_2O$ and anatase seems to be slightly better than the titanate nanotubes reported by [126, 127, 128]. However, Sandoval *et al.* [125] seem to have produced a superior mixed structure of $Na_2Ti_3O_7$ and $H_2Ti_3O_7$ nanotubes.

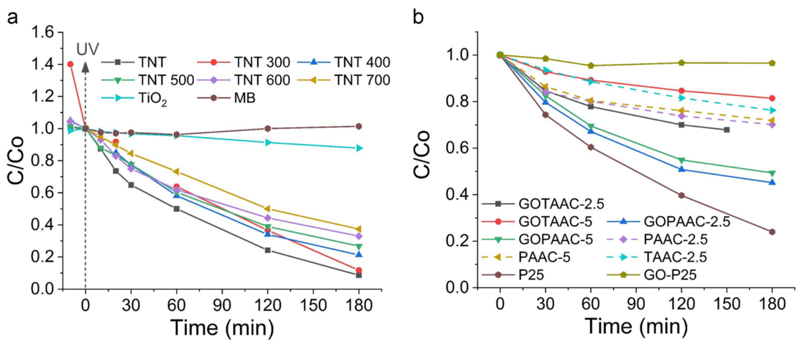


**Figure 3.6.** Decolorization of MB using a) titanate nanotubes and b) GO/$TiO_2$/Ag/AgCl composites under UV light irradiation. Adapted from Publication I and Publication III.

$TiO_2$ coupled with graphene derivatives are reported as efficient photocatalysts, as compared to pristine $TiO_2$. The graphene loadings in these photocatalysts are significantly lower, i.e. 0.25 wt.% up to a maximum of 20 wt.% [77, 129, 130], of which the most efficient photocatalyst generally has a graphene concentration less than 5 wt.%. In this work, the effect of a larger nominal weight percent of GO was studied in the GO/$TiO_2$/Ag/AgCl composites. The decolorization of MB under UV-light irradiation was studied for the GO/$TiO_2$/Ag/AgCl, and compared to the corresponding $TiO_2$/Ag/AgCl composites, as well as Degussa P25 and a GO-P25 composite. All composite powders, except GO-P25, showed photocatalytic decolorization of MB under UV-light irradiation, however, the commercially available Degussa P25 $TiO_2$ photocatalyst was the most efficient, shown in Fig. 3.6b. The quaternary composites using Degussa P25 $TiO_2$, i.e. GOPAAC-2.5 and GOPAAC-5, displayed the highest photocatalytic efficiency of the composites. The difference in the photocatalytic activity between the GOPAAC and GO-P25 composites after such a large adsorption prior to irradiation was intriguing. Both composites use 50 wt.% GO, and P25 as $TiO_2$ source, but the GOPAAC composites have an added Ag/AgCl part, which must have played an active role in the photocatalysis. Also, the role of GO in the decreased photocatalytic efficiency in the GO-P25 composite was examined, as compared to pristine P25 $TiO_2$. The only difference between the pristine P25 and GO-P25 composites was the GO content. The GO was suggested to affect the efficiency by hindering the light from arriving at the $TiO_2$ surface due to the large adsorption of MB, which hinders the photocatalytic reactions from taking place. The large concentration of GO (50 wt.%) in the GO/$TiO_2$/Ag/AgCl caused the GO to stack in a graphite like structure due to the strong $\pi-\pi$ interactions between the GO sheets, which reduces the active surface area. However, both GOPAAC and GO-P25 composites contain the same amount of GO, so the Ag/AgCl-part in the GOPAAC composites had to have an effect on the activity as well. AgCl is a semiconductor with an indirect bandgap of 3.25 eV [131]. It was suggested that the AgCl is decomposed to $Ag^+$ and $Cl^-$ under UV-light. These undergo further reactions creating e.g. superoxide radicals ($O_2{}^-\cdot$) [132], and would thus act as a charge separator aiding the photocatalytic reactions. The AgCl would eventually be reduced to Ag, which is active under visible light [67, 132]. The GO part had to have some other effect in the photocatalysis since the GOPAAC composites showed enhanced photocatalytic degradation as compared to the GO-free PAAC composites. The proposition is that GO also acts as a charge separator in the GOPAAC composites. As charge carriers (electrons and holes) were generated, GO would reduce and functional oxygen groups from the surface would be removed. The released oxygen species then take part in the decoloration of MB. The reduction of GO would also cause a band gap reduction and increase the electron conductivity, which prolongs the lifetime of the photogenerated electrons. Finally, the GOPAAC outperformed GOTAAC composites due to the favorable anatase to rutile ratio and the hydroxyl groups in P25 $TiO_2$, as compared to the in-house made $TiO_2$.

Not many four-component photocatalysts have been reported containing similar materials. Pan *et al.* [86] report a AgCl@Ag/TNT/N-RGO photocatalyst and Wang *et al.* [85] report a Ag-AgBr/$TiO_2$/RGO photocatalyst and both studies were conducted under visible light irradiation. The loading of GO is not reported. It is problematic to compare the photocatalytic degradation results, as they were made with RhB or Penicillin G model pollutants under visible light irradiation. Both AgCl@Ag/TNT/N-RGO and Ag-AgBr/$TiO_2$/RGO were efficient photocatalysts and were able to degrade the probed pollutants in less than 120 minutes of irradiation. To conclude, the GO/$TiO_2$/Ag/AgCl composites reported herein might not be as efficient photocatalysts as the ones using smaller amounts of GO [77, 129, 130]. Most studies do not complete adsorption before irradiation, which affects the photocatalytic efficiency significantly as the outcome then reports both the adsorption and the photocatalytic degradation combined. Herein, the adsorption and photocatalysis are separated for all GO/$TiO_2$/Ag/AgCl composites. In addition, since the GO/$TiO_2$/Ag/AgCl has a visible light active part, it would be of interest to investigate the photocatalytic efficiency under visible light.

The photocatalytic performance of the RBA TNT samples was evaluated by using MO and RhB as model pollutants and studied under both UV- and natural sunlight. It is important for photocatalysts to be able to utilize a wider range of the solar light spectrum than only UV-light. The photocatalytic efficiency of the whole spectrum of the sun is identified by first distinguishing the efficiency under UV light. The RBA TNT samples showed decolorization of the MO dye up to 47 % and RhB dye up to 43 % under UV-light irradiation after 3 h of irradiation, however, the anatase $TiO_2$ reference powder was superior with complete decolorization under UV light, shown in Figs. 3.7a and b. RBA TNTs have been studied before under UV-light rendering faster decolorization of MO [49] and Acid Orange 7 [50]. Figs. 3.7c and d show the decolorization of MO and RhB under natural sunlight using the TNT powders. The reference anatase powder performed identically under both UV- and sunlight irradiation, which was attributed to the UV-light in the natural sunlight, as the band gap was in the UV-light range (3.2 eV). This implies that if all samples would get identical results under both light sources, they would only use UV-light efficiently. However, all TNT powders showed increased photocatalytic decolorization efficiency under natural sunlight, as compared to under UV-light.

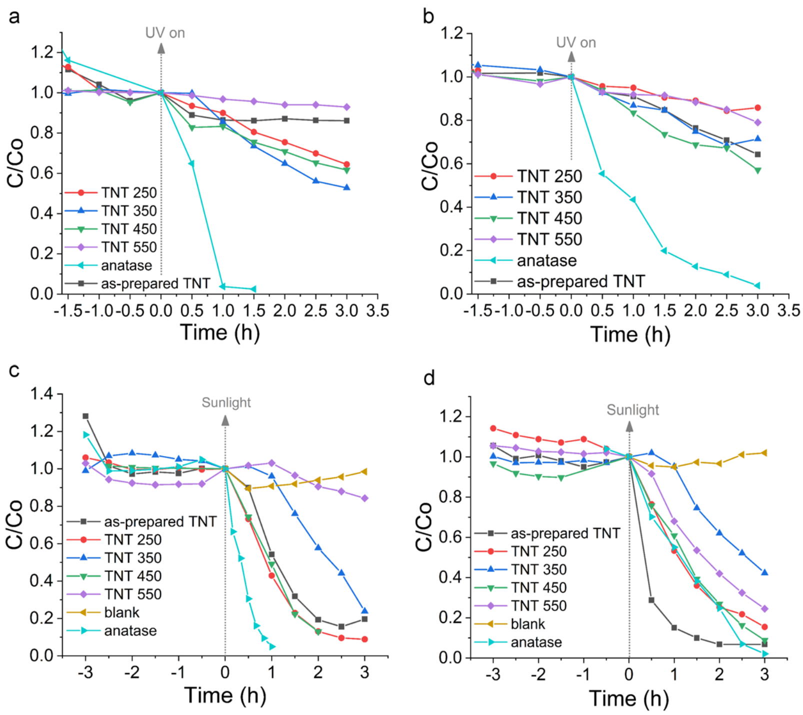


**Figure 3.7.** Photocatalytic decolorization of a) MO and b) RhB under UV light and c) MO and d) RhB under natural sunlight irradiation using rapid breakdown andodized titania nanotubes. Adapted from Publication II.

The as-prepared TNT, TNT 250 and TNT 450 samples were the most excellent photocatalysts of the TNT samples. The main differences between these samples were in their structure, specific surface area, incident photon to photocurrent efficiency (IPCE) values and degree of impurities. The as-prepared and TNT

250 samples consisted of anatase phase and had a tubular structure with high surface area. In TNT 450, the tubular structure had collapsed to rods, and displayed both anatase and brookite phases, and showed low recombination and better conductivity, as obtained from the IPCE values. No photocurrent could be collected possibly due to the higher amount of chlorine impurity in the as-prepared TNT and TNT 250 samples. The PL results suggested a better electron-hole separation in TNT 450 as compared to the as-prepared sample. The TNT samples also had an abundance of -OH groups up to 450 °C, however the amount of -OH groups decreased upon annealing (Fig. 3.4b). As mentioned earlier, the -OH groups participate in the photocatalytic reactions and absorption of the dye on the photocatalyst surface, which is crucial for the photocatalytic degradation to take place. All these properties of the samples participate synergistically to improve the photocatalytic efficiency. The degradation of RhB using RBA rutile nanotubes under visible light irradiation obtained a decoloration efficiency up to 80 % [53], which is lower than the almost complete decolorization herein. However, the study by Savitha *et al.* [53] was conducted under only visible light irradiation.

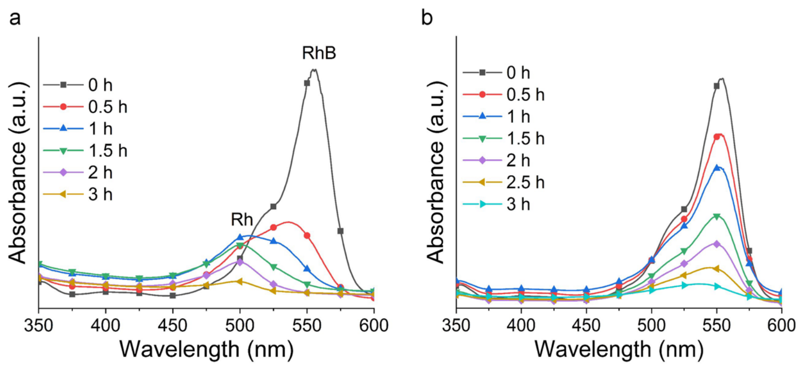


**Figure 3.8.** UV-Vis absorption spectra of the decolorization of RhB using a) as-prepared TNT and b) TNT 450 under natural sunlight irradiation. Rh marks the peak for Rhodamine and RhB for Rhodamine B. Adapted from Publication II.

It was observed that the degradation mechanism of RhB was different for the as-prepared TNT sample when compared to the other samples. There were two types of changes observed, i.e., RhB absorbance decreased and the peak shifted to 498 nm. The as-prepared TNT sample decolorized RhB following the trend in Fig. 3.8a, whereas the other samples followed the trend in Fig. 3.8b. All samples followed the route in Fig. 3.8b under UV-light irradiation. The new peak at 498 nm in Fig. 3.8a was identified as Rhodamine (Rh), which is an N-de-ethylation product of RhB [133, 134]. This takes place when RhB is excited under visible light and transfers the excited electrons to the conduction band of the as-prepared TNT powder. As no other photocatalysts displayed this behavior, the difference had to be in the characteristics of the as-prepared TNT sample. N-de-ethylation of RhB has been observed for titanate nanotubes under simulated solar light, however, this phenomenon was not observed for the corresponding nanowires [47]. The N-de-ethylation reaction on the as-prepared TNT powder was thus attributed to a higher adsorption of RhB, due to the higher amount of oxygen functional groups, and higher surface area, as the N-de-ethylation reaction is dependent on the formation of OOH· and OH·.

## 3.2 Properties of $SiO_2$-Ag composites

This section focuses on the morphology and structure of the $SiO_2$-Ag composites. The growth of silver particles is studied and the effectiveness of the $SiO_2$-Ag 300 composite in an antibacterial application is evaluated.

### 3.2.1 Morphology and structure

The morphology and structure of the $SiO_2$-Ag composites were determined, followed by a study of the growth and dissolution of silver (PIV). The shape of the $SiO_2$-Ag composite clusters or agglomerates was studied by SEM imaging. Fig. 3.9 shows the cluster shape for $SiO_2$-Ag 600 and $SiO_2$-Ag 700, however, all $SiO_2$-Ag samples displayed this irregular shape made up from aggregated spheres in various sizes.

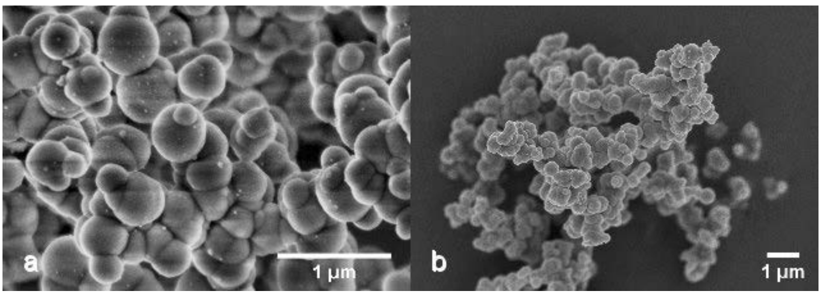


**Figure 3.9.** Scanning electron micrographs of a) $SiO_2$-Ag 600 and b) $SiO_2$-Ag 700. Both scale bars are 1 $\mu$m.

The crystallinity of Ag in the $SiO_2$-Ag composites was examined. The XRD patterns revealed diffraction peaks for Ag in the $SiO_2$-Ag 600, $SiO_2$-Ag 700 and $SiO_2$-Ag 800 samples, however, no Ag peaks were observed at heat treatment temperatures below 600 °C (PIV, Fig. 2) . The silver particles were presumed to be crystalline in all the heat treated samples, and therefore selected area electron diffraction (SAED) was employed for the $SiO_2$-Ag 300 sample. SAED revealed clear ring patterns, which corresponded to the d-spacings of silver (PIV, Fig. 4). The atomic state of silver was also examined by XPS, which also confirmed metallic state of silver in all $SiO_2$-Ag composites (PIV, Fig. 5). The TEM images affirmed that Ag NPs were located both inside and on top of the $SiO_2$ matrix (PIV, Fig. 2).

### 3.2.2 Growth of silver nanoparticles

The growth of silver particles was studied by annealing the $SiO_2$-Ag composite at 300-800 °C for a constant time of 75 minutes. The Ag particle size plays a large role in the antibacterial properties, as smaller Ag NPs below 10 nm in size have shown increased antibacterial activity as compared to larger ones [101]. This effect may be attributed to the increase in the surface area to volume ratio and realtive particle concentration, when the particle size decreases. The mean size of the Ag particles inside and on the surface of the $SiO_2$ matrix was determined from a number of SEM and TEM images by using the ImageJ measurement tool from selected areas in the chosen images. The Ag particle size measurements for the as-prepared $SiO_2$-Ag composite powder was solely made from TEM images due to the small size of the silver particles (PIV), as well as for $SiO_2$-Ag 300 in PV .

The statistics of the size distribution of silver are shown in Fig. 3.10. Fig. 3.11 depicts the mean Ag NP sizes with the standard deviation as error bars. The Ag particles were only measured from the surface when using SEM images, as the method only displays the surface of the powders. Also, only larger particles could be measured since the resolution of the SEM restricted the measurement of smaller particles. The smaller particle sizes were obtained from high-resolution TEM images, from both the surface and the inside of the $SiO_2$ matrix. The combination of the two measurements is represented in Fig. 3.11b. The trend in all cases was that the particle size increased with higher heat treatment temperature, independent of the imaging method. Noteworthy was the large standard deviation, which indicated broad size distributions. Table 3.1 and Fig. 3.10 shows the Ag sizes and size distribution measured and calculated from both SEM and TEM images. The Ag size distribution broadened when the heat treatment temperature increased, as demonstrated by the particle size distribution statistics. This type of representation does, however, consider Gaussian curve-fit and division of sizes. The Ag particles appeared to grow more freely in size on or near the surface of the $SiO_2$ matrix, and at higher temperatures, some Ag particles desquamated from the surface of $SiO_2$. The Ag particles which were smaller in size were found inside the $SiO_2$ matrix.

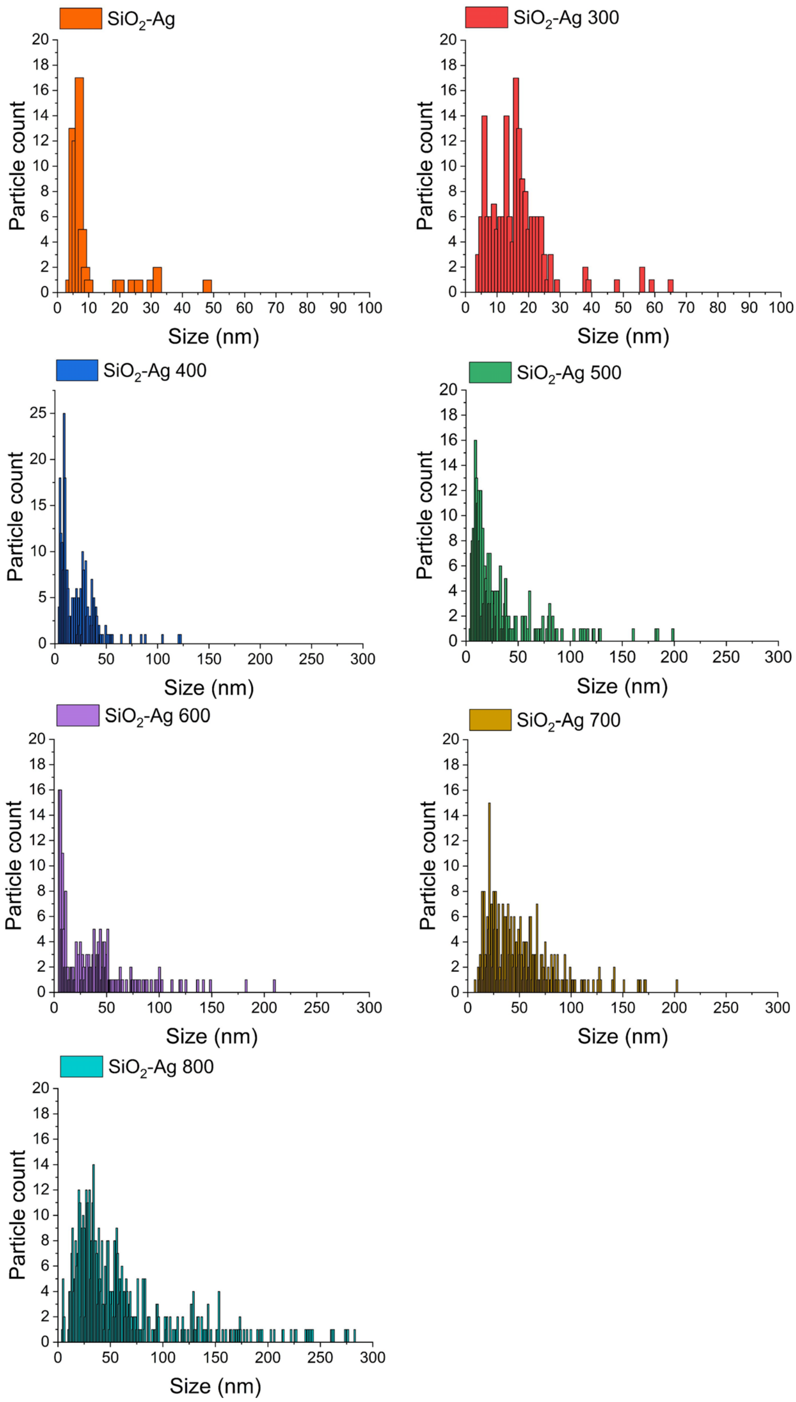


**Figure 3.10.** The statistics for silver particle size distribution in all $SiO_2$-Ag composites.

**Table 3.1.** Statistics of silver nanoparticle sizes, amount of measured particles (N total) and their standard deviation (SD) measured and calculated from both SEM and TEM images with the exception of the as-prepared sample (RT= room temperature), which were only measured from TEM images. Q1 and Q3 stand for first quartile and third quartile, respectively.

| **T** | **N total** | **Mean** | **SD** | **Min** | **Q1** | **Median** | **Q3** | **Max** |
|---|---|---|---|---|---|---|---|---|
| (°C) | particles | (nm) | (nm) | (nm) | (nm) | (nm) | (nm) | (nm) |
| RT | 60 | 10 | 9 | 4 | 6 | 7 | 8 | 48 |
| 300 | 175 | 16 | 10 | 4 | 10 | 16 | 20 | 65 |
| 400 | 186 | 25 | 20 | 4 | 10 | 22 | 32 | 122 |
| 500 | 247 | 30 | 33 | 4 | 10 | 18 | 35 | 199 |
| 600 | 188 | 28 | 36 | 4 | 9 | 31 | 50 | 210 |
| 700 | 298 | 50 | 33 | 7 | 25 | 42 | 66 | 202 |
| 800 | 495 | 61 | 54 | 4 | 27 | 42 | 73 | 283 |

The silver particle size was remeasured for $SiO_2$-Ag 300 (PV). The mean particle size of 5 nm was obtained, with a standard deviation of 2 nm. The maximum Ag size was 20 nm and minimum size was 2 nm. However, these particle measurements were only obtained from TEM images, and therefore some size differences may arise from the area of which silver particles were measured. Some differences in Ag size might also arise from different batches. The method does not restrict the amount of incorporated silver and the amount of silver remaining in the solution, due to the absence of reducing agent. However, the resulting Ag particle size still remained in the smaller range.

The growth was further studied by determination of the activation energy of Ag particle growth. This was carried out by using a linear fit of the mean Ag particle sizes in an Arrhenius type plot, as the growth seemed to be temperature dependent. The linear fit in Fig. 3.11a is fitted following the equation:

$$ln(D - D_0) = \frac{-Q_A}{k_B T} + A^t, \tag{3.1}$$

where D is the particle size, $D_0$ is the particle size at t= 0, and $A^t$ is a constant. The activation energy, $Q_A$, for Ag particle growth was then obtained from the slopes. The $Q_A$ for the Ag particles from both SEM and TEM images was 0.14 eV. Further, the growth of silver particles inside the $SiO_2$ matrix might require more energy, due to the $SiO_2$ network hindering the movement of silver. This indicates that there might be two growth mechanisms through diffusion present in the $SiO_2$-Ag composites. The Ag particles on top of the $SiO_2$ surface seemed to grow on the cost of smaller ones, and thus the growth mechanism was described by Ostwald ripening. The diffusion of silver inside the $SiO_2$ matrix is obviously more difficult and the particle growth is slower and would require additional experiments to determine in detail. Activation energies of silver particle growth in the range of 0.064-5.2 eV have been reported before for silver particle growth in silica films [88, 135, 136, 137]. However, the processing conditions in above references were are different, i.e., different temperature ranges and heat treatment times and the studies were made in silica films with various silver impregnation methods.

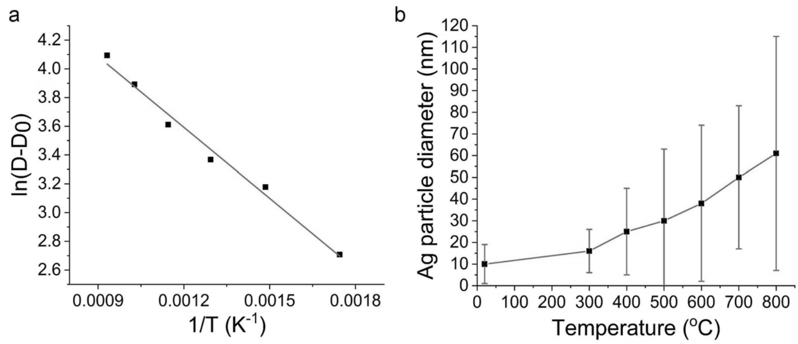


**Figure 3.11.** (a) An Arrhenius type plot for determination of activation energy ($Q_A$) for Ag NP growth on the $SiO_2$ matrix. The plot is calculated using Ag NP diameter measurements from both SEM and TEM images. (b) The mean Ag NP sizes and standard deviations (error bars) measured from both SEM and TEM images. The graph in a) is adapted from Publication IV.

### 3.2.3 Dissolution of silver

The release of silver from a selection of $SiO_2$-Ag composites was studied to obtain the concentration and release of silver from the surface and potentially from inside the matrix $SiO_2$ of the composites. The $SiO_2$-Ag 300, $SiO_2$-Ag 600 and $SiO_2$-Ag 700 powders were examined for 1, 3 and 7 days time in de-ionized water at room temperature (RT), at 40 °C and 60 °C, as well as at pH 4 and pH 10 in pH adjusted de-ionized water at RT. The pH was adjusted using $HNO_3$ and NaOH. The results are shown in Fig. 3.12.

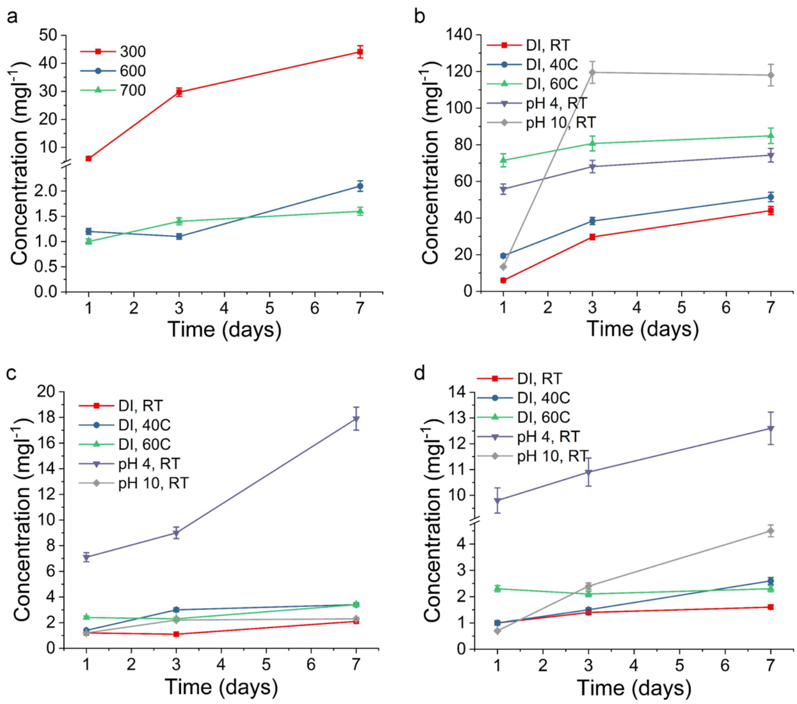


**Figure 3.12.** The silver release from a) $SiO_2$-Ag 300, $SiO_2$-Ag 600 and $SiO_2$-Ag 700 in de-ionized (DI) water at room temperature (RT) for 7 days. The release of silver for b) $SiO_2$-Ag 300, c) $SiO_2$-Ag 600, and d) $SiO_2$-Ag 700 for up to 7 days time at RT, at 40 °C, 60 °C, pH 4 and pH 10. Reproduced from Publication IV.

The release of Ag from the $SiO_2$-Ag composites increased typically with longer dissolution time and stagnated only in a few cases after 3 days dissolution time. The largest concentration of Ag species into the solutions was attained by the $SiO_2$-Ag 300 composite powder. The higher dissolution concentrations of $SiO_2$-Ag 300 is likely due to the smaller Ag particle size, which provides a larger surface area for dissolution. Control samples were prepared to acquire the maximum level of Ag dissolution from each sample. The tests revealed that up to 74 % of the theoretical maximum concentration of Ag in the powders could be leached. However, a maximum of 38 % was in fact dissolved from the surface, compared to the control tests. This indicated that there was a significant amount of Ag still to be released after the 7 dissolution days.

Another dissolution test for $SiO_2$-Ag 300 was examined for 3 days. The dissolution was carried out in purified water for 0 to 3 days. The trend remained the same, i.e., the dissolution increased with longer dissolution times. The powders could be examined for even longer times since a plateau in the Ag release was not reached within the examined time. The dissolution tests provided important implications for the antibacterial tests, as a sustained dissolution of Ag is essential for prolonged antibacterial effects.

### 3.2.4 Antibacterial properties

The increased concentration in dissolved silver species provided by dissolution tests indicated that prolonged release of silver was possible for the use in antibacterial applications. The $SiO_2$-Ag 300 composite was chosen for the antibacterial tests due to the small silver particle size (~5 nm), as small silver nanoparticles have been shown to be more efficient antibacterial agents [101]. The $SiO_2$ matrix reduced the agglomeration of silver nanoparticles and it may also facilitate extended leaching of Ag, i.e., provide a prolonged antibacterial effect. The $SiO_2$-Ag 300 composite was investigated in agar diffusion assays in both powder form and impregnated in wound dressings. The antibacterial mechanism was studied by examining the destruction of MRSA bacteria cells.

UV-sterilization and filter-sterilization methods were investigated to preserve the antibacterial efficacy of the $SiO_2$-Ag 300 composite. Antibacterial susceptibility tests were performed on *E. coli* and MRSA in agar diffusion assays using the $SiO_2$-Ag 300 composite, and $SiO_2$ particles for comparison. The antibacterial effect was studied by measuring IZs from the bacteria containing plates. The UV-sterilized $SiO_2$-Ag 300 composite generated larger IZs for both bacteria in the agar diffusion assays, which is due to a higher retained Ag concentration of the composite when using UV-sterilization. Most of the composite powder is stuck in the filter when using the filter-sterilization technique due to the large $SiO_2$ agglomerate size, whereas in UV-sterilization all of the composite powder is retained. Therefore, UV-sterilization was concluded to be the more suitable method in this case. The reference $SiO_2$ particles did not inhibit the growth of bacteria. This result implied that Ag played an active role in the antibacterial effect, whereas $SiO_2$ did not. As both Gram-positive MRSA and Gram-negative *E. coli* types of bacteria were tested and $SiO_2$-Ag 300 showed growth inhibition for both, it is possible to use the composite for wound infection prevention, as both types are associated with wound infections.

The second set of agar diffusion assays were prepared for wound dressing applications with a gauze soaked in a suspension containing the $SiO_2$-Ag 300 composite ($Ag-SiO_2-G$). The results were consistent with the results obtained for the composite powder, that is the $Ag-SiO_2-G$ was effective against both MRSA and *E. coli*. The results were verified by comparing to a control gauze without silver, which did not hinder bacterial growth. The results were also compared to a commercial silver dressing (CSD), however, the CSD did not inhibit the growth of MRSA and only slightly in the case of *E. coli* and the IZs formed by the CSD were smaller than the IZs for the $Ag-SiO_2-G$.

The minimum inhibitory concentrations (MICs) were 250 $\mu$g/mL and 500 $\mu$g/mL against MRSA and *E. coli* using the $SiO_2$-Ag 300 composite, respectively. By correlation of this result to the silver release study in section 3.2.3, the Ag concentrations were determined as ca 5.5 $\mu$g/mL and 11 $\mu$g/mL Ag in the suspensions, for MRSA and *E. coli*, respectively. The MICs were smaller than those previously reported [115, 138], which suggests a higher efficiency in hindering bacterial growth. These results implicated that the $SiO_2$-Ag 300 composite was effective against both Gram-positive and Gram-negative bacteria.

The prolonged antibacterial effect of the $Ag-SiO_2-G$ was also investigated in turbidity assays. A prolonged antibacterial effect is desired for e.g. a less frequent wound dressing change [139]. The $Ag-SiO_2-G$ hindered bacterial growth after 24 h and reduces the growth even after 48 h, which clearly indicates a prolonged antibacterial effect.

The antibacterial action of the silver nanoparticles in the $SiO_2$-Ag 300 composite was analyzed by TEM to be able to distinguish the antibacterial mechanisms of silver on the bacterial cells [98]. Fig. 3.13 shows the morphological changes in MRSA treated with the $SiO_2$-Ag 300 composite. MRSA and MRSA treated with $SiO_2$ particles are shown in Figs. 3.13a-b for comparison. The antibacterial action was shown to include; gaps between the cell walls and cytoplasmic membrane (green arrows), the release of cytoplasmic content from the bacterial cells (orange arrows), central condensation of the bacteria DNA (blue arrow), and breakage and loss of the bacterial membrane (red arrows). From these observations, it was possible to conclude that the antibacterial effect is due to the released $Ag^+$ from the $SiO_2$-Ag 300 composite. The $Ag^+$ can permeate the bacterial cells and interact inside the bacteria. $Ag^+$ is also suggested to hinder the replication ability in the bacteria, which was shown by the condensation of DNA. The interaction of $Ag^+$ with the thiol groups in the bacterial proteins renders them inactive, and thus damages or destroys the cell wall [100, 140].

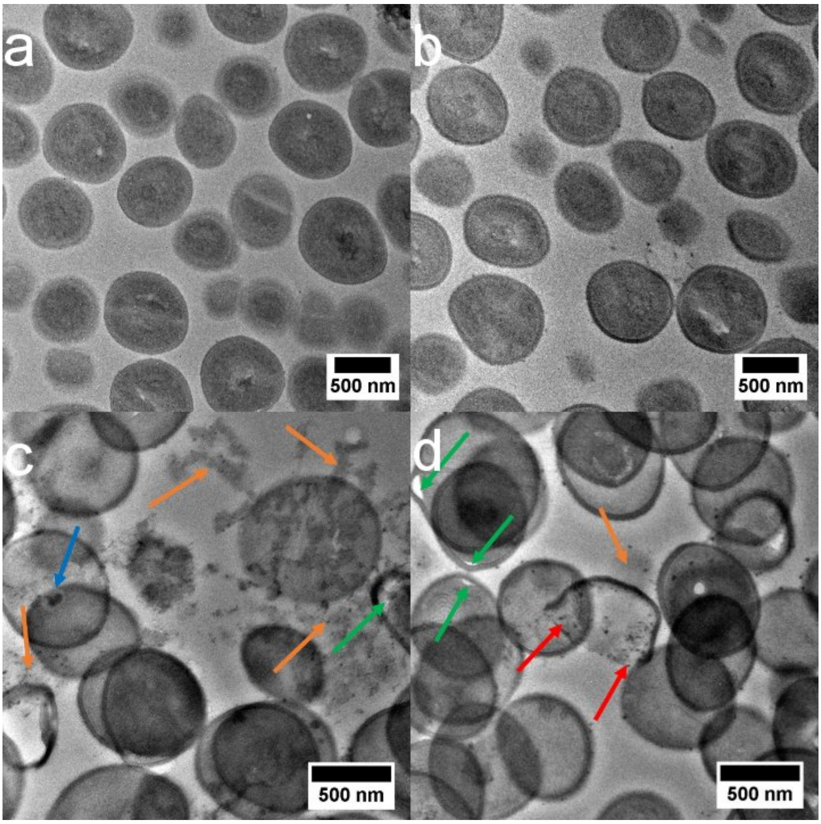


**Figure 3.13.** TEM images of a) MRSA, b) MRSA treated with $SiO_2$ particles and c)-d) MRSA treated with the $SiO_2$-Ag 300 composite. Green arrows: gaps between the cell walls and cytoplasmic membrane; Orange arrows: the release of cytoplasmic content from the bacterial cells; Blue arrow: central condensation of the bacteria DNA; Red arrows: breakage and loss of the bacterial membrane. Reproduced with modifications from PV.

# 4. Conclusions and future outlook

The aim in this thesis was to develop means to counteract harmful organic contaminants and bacteria in our habitat. The focus was placed on titania as high-efficiency photocatalysts for organic contaminants removal and on silica-silver composites for antibacterial purposes. Based on the results presented in this compilation and the appended publications, the following conclusions can be drawn:

- Titanate nanotubes prepared by reflux heating under alkaline conditions were shown to consist of anatase crystalline phase and of $Na_xH_{2-x}Ti_3O_7 \cdot H_2O$ without post-treatment. Post-synthesis annealing at 300-450 °C retained the tubular morphology. The tubular morphology collapsed to nanorods above 450°C. The tubes were completely transformed into nanorods at 600 °C. The crystal structure also changed at 600 °C from a mixture of $Na_xH_{2-x}Ti_3O_7 \cdot nH_2O$ and anatase to a mixture of $Na_2Ti_6O_{13}$ and anatase phase. The increase in annealing temperature removed hydroxyl surface functional groups. The annealing of the titanate nanotubes was directly related to the change in crystal structure and decreased the surface area due to the collapse of the tubular structure. The band gaps for all titanate tubes were around 3.1 eV, which is close to the visible light range.

- Titania nanotubes were prepared by rapid breakdown anodization in a perchloric acid and subjected to post-treatment by annealing at 250-550 °C. The as-prepared nanotubes were in anatase phase, which transformed into an anatase/brookite phase mixture at 450 °C and further into anatase/rutile phase mixture at 550 °C. These nanotubes retained the nanotubular structure up to 250 °C, after which they transformed into rods and further collapsed to form particles at 550 °C. The amount of hydroxyl surface groups decreased and the surface area was reduced due to the collapse of the tubular structure upon annealing at higher temperatures, similar to the titanate nanotubes case. A shift in band gap to the visible light range was evident for the sample annealed at 550 °C.

- The photocatalytic properties of the titanate nanotubes were investigated under UV-light irradiation using MB as model pollutant. The photocatalytic decolorization of the MB dye decreased with increasing annealing temperature, and the as-prepared TNT sample outperformed the in-house made reference $TiO_2$ powder. The increase in photocatalytic decolorization when using the as-prepared TNT sample was due to the high amount of hydroxyl surface groups and high surface area.

- The photocatalytic efficiency of the titania nanotubes prepared by rapid breakdown anodization was examined both under UV-light and natural sunlight irradiation using RhB and MO as model pollutants. The photocatalytic degradation of both dyes was enhanced under natural sunlight irradiation, even though the band gaps were at the UV- and visible light boundary. The as-prepared TNT outperformed the commercial reference anatase $TiO_2$ powder, but only using RhB under natural sunlight. The as-prepared TNT sample and the samples annealed at 250 °C and 450 °C were the most prominent photocatalysts of the nanotubes powder samples. The photocatalytic efficiency was proposed to be due to a synergistic effect of surface area, -OH groups, crystal structure, and charge carrier formation.

- Quaternary nanocomposites consisting of GO, $TiO_2$, Ag and AgCl were prepared using a high GO content of 50 wt.%. The effect of the titania source and the concentration of reducing agent was investigated for photocatalyst structure optimization. In-house made anatase $TiO_2$ and commercial Degussa P25 $TiO_2$ powders were included as titania sources in the composites, whereas PVP was used in two different concentrations to form silver particles. A higher degree of separation of GO sheets was observed in the composites containing Degussa P25 $TiO_2$. The relative amount of AgCl and the anatase to rutile ratio were different for the composites using different titania sources. No significant difference in the composite structure was observed when using different concentrations of PVP.

- The adsorption and photocatalytic efficiency of the GO/$TiO_2$/Ag/AgCl nanocomposites were examined by decolorizing MB under UV-light irradiation. A significant adsorption of MB onto the GO sheets was observed due to the large surface area of GO, which provided adsorption sites for the MB dye. The addition of GO to the GO/$TiO_2$/Ag/AgCl composites enhanced the photocatalytic decolorization of MB, compared to the respective $TiO_2$/Ag/AgCl composites. However, the reduction of the GO sheets under UV-light rendered the photocatalyst inactive after sufficient time, as the advanced oxidation reactions involved in photocatalysis are dependent on reactive oxygen species. The Ag/AgCl part is suggested to function as charge separators, enhancing the decolorization efficiency.

- $SiO_2$-Ag composites were prepared by a modified Stöber method and heat treated at 300-800 °C for 75 minutes. The synthesis procedure was free of reducing agents and the growth of the silver particles was tuned during the heat treatment. The growth of silver nanoparticle size was studied by electron microscopy techniques and the activation energy for particle growth determined as 0.14 eV. The dissolution of Ag from the composites annealed at 300 °C, 600 °C and 700 °C was investigated in aqueous solutions from room temperature to 60 °C, and at different pH for 1 to 7 days. The dissolution of silver from the composites increased with longer dissolution times, and the release was higher for smaller particle sizes.

- The $SiO_2$-Ag composite heat treated at 300 °C for 75 minutes was chosen for antibacterial tests due to the small silver particle size and the encouraging results acquired from the dissolution tests. The composite was effective against both studied bacteria, i.e. MRSA and *E. coli*, when studied in vitro. Two sterilization methods for the $SiO_2$-Ag composite powder were studied, namely UV-sterilization and filter sterilization, and UV-sterilization was found superior in this case. The $SiO_2$-Ag composite was also impregnated in wound dressings and showed a higher antibacterial efficiency than a commercial silver-containing dressing. The antibacterial mechanism of silver in MRSA bacteria was also studied and several antibacterial mehanisms were observed, which eventually lead to the destruction of the bacterial membrane and release of the cytoplasmic content of the bacteria. The prolonged release of silver from the prepared dressing reduced the bacterial growth.

The photocatalyst field is very competitive, and titania is probably the most studied material. However, future investigations should focus on upscaling the production of the high-efficiency photocatalyst structures and making them applicable in large scale in natural environments. The presented RBA method provides a facile and cost-efficient way of making titania nanotubes powder for photocatalytic applications, however, the structure still needs optimization for more efficient visible light absorption, which can be achieved by doping or formation of composite structures. Investigations like these could make the photocatalyst application practical and ensure clean water for everyone.

The $SiO_2$-Ag composites are very versatile. The growth of silver should be studied in more detail and differences between the growth of Ag on the $SiO_2$ surface and inside the $SiO_2$ matrix for variable times at different temperatures must be investigated. It would also be of interest to study the release of silver from the $SiO_2$ matrix over a long period of time. These two studies would provide more optimized control of Ag size for the use in antibacterial applications. Further investigations of the already studied $SiO_2$-Ag composite on the cytotoxicity in skin cells are crucial for commercializing a wound dressing product. Impregnation in other kinds of wound dressings and study of the wound healing properties of the $SiO_2$-Ag composite in vivo are also of interest. Depending on these future results, topical antibiotics could possibly be completely excluded from wound care.

# References


[1] T. Loudenback, "The 10 biggest problems in the world today, according to millennials," *Business Insider*, August 2016.

[2] M. Shannon, P. Bohn, M. Elimelech, J. Georgiadis, B. Marĩas, and A. Mayes, "Science and technology for water purification in the coming decades," *Nature*, vol. 452, no. 7185, pp. 301–310, 2008.

[3] Y. Xiao, J. Wu, G. Yue, G. Xie, J. Lin, and M. Huang, "The preparation of titania nanotubes and its application in flexible dye-sensitized solar cells," *Electrochimica Acta*, vol. 55, no. 15, pp. 4573–4578, 2010.

[4] B. Lyson-Sypien, A. Czapla, M. Lubecka, E. Kusior, K. Zakrzewska, M. Radecka, A. Kusior, A. Balogh, S. Lauterbach, and H.-J. Kleebe, "Gas sensing properties of $TiO_2$–$SnO_2$ nanomaterials," *Sensors and Actuators B: Chemical*, vol. 187, pp. 445 – 454, 2013.

[5] N. Abidi, L. Cabrales, and E. Hequet, "Functionalization of a cotton fabric surface with titania nanosols: Applications for self-cleaning and UV-protection properties," *ACS Applied Materials and Interfaces*, vol. 1, no. 10, pp. 2141–2146, 2009.

[6] C. Arunchandran, S. Ramya, R. George, and U. Mudali, "Self-healing corrosion resistive coatings based on inhibitor loaded $TiO_2$ nanocontainers," *Journal of the Electrochemical Society*, vol. 159, no. 11, pp. C552–C559, 2012.

[7] P. Roy, S. Berger, and P. Schmuki, "$TiO_2$ nanotubes: Synthesis and applications," *Angewandte Chemie - International Edition*, vol. 50, no. 13, pp. 2904–2939, 2011.

[8] X.-J. Zhang, T.-Y. Ma, and Z.-Y. Yuan, "Titania-phosphonate hybrid porous materials: Preparation, photocatalytic activity and heavy metal ion adsorption," *Journal of Materials Chemistry*, vol. 18, no. 17, pp. 2003–2010, 2008.

[9] L. Preethi, R. P. Antony, T. Mathews, S. Loo, L. H. Wong, S. Dash, and A. Tyagi, "Nitrogen doped anatase-rutile heterostructured nanotubes for enhanced photocatalytic hydrogen production: Promising structure for sustainable fuel production," *International Journal of Hydrogen Energy*, vol. 41, no. 14, pp. 5865 – 5877, 2016.

[10] L. Preethi, T. Mathews, M. Nand, S. Jha, C. S. Gopinath, and S. Dash, "Band alignment and charge transfer pathway in three phase anatase-rutile-brookite $TiO_2$ nanotubes: An efficient photocatalyst for water splitting," *Applied Catalysis B: Environmental*, vol. 218, pp. 9 – 19, 2017.

[11] H. Honda, A. Ishizaki, R. Soma, K. Hashimoto, and A. Fujishima, "Application of photocatalytic reactions caused by $TiO_2$ film to improve the maintenance factor of lighting systems," *Journal of the Illuminating Engineering Society*, vol. 27, no. 1, pp. 42–49, 1998.

[12] A. Fujishima, X. Zhang, and D. A. Tryk, “$TiO_2$ photocatalysis and related surface phenomena,” *Surface Science Reports*, vol. 63, no. 12, pp. 515 – 582, 2008.

[13] A. Di Paola, M. Bellardita, and L. Palmisano, “Brookite, the least known $TiO_2$ photocatalyst,” *Catalysts*, vol. 3, no. 1, pp. 36–73, 2013.

[14] Q. Zhang, Y. Zhou, Z. Zhang, Y. He, Y. Chen, and Y. Lin, “Plasmonic photocatalyst,” *Progress in Chemistry*, vol. 25, no. 12, pp. 2020–2027, 2013.

[15] B. Ohtani, O. Prieto-Mahaney, D. Li, and R. Abe, “What is Degussa (Evonik) P25? Crystalline composition analysis, reconstruction from isolated pure particles and photocatalytic activity test,” *Journal of Photochemistry and Photobiology A: Chemistry*, vol. 216, no. 2, pp. 179 – 182, 2010. 3rd International Conference on Semiconductor Photochemistry, SP-3, April, 2010, Glasgow UK.

[16] “718467 ALDRICH Titanium(IV) oxide,” *Sigmaaldrich.com*, 2018. Accessed on 6.3.2018.

[17] D. C. Hurum, A. G. Agrios, K. A. Gray, T. Rajh, and M. C. Thurnauer, “Explaining the enhanced photocatalytic activity of Degussa P25 mixed-phase $TiO_2$ using EPR,” *The Journal of Physical Chemistry B*, vol. 107, no. 19, pp. 4545–4549, 2003.

[18] S. Ali and S.-P. Hannula, “Titania nanotube powders obtained by rapid breakdown anodization in perchloric acid electrolytes,” *Journal of Solid State Chemistry*, vol. 249, pp. 189 – 198, 2017.

[19] A. Kachina, E. Puzenat, S. Ould-Chikh, C. Geantet, P. Delichere, and P. Afanasiev, “A new approach to the preparation of nitrogen-doped titania visible light photocatalyst,” *Chemistry of Materials*, vol. 24, no. 4, pp. 636–642, 2012.

[20] A. Ramchiary and S. Samdarshi, “Ag deposited mixed phase titania visible light photocatalyst - Superiority of Ag-titania and mixed phase titania co-junction,” *Applied Surface Science*, vol. 305, pp. 33–39, 2014.

[21] P. Cheng, W. Li, T. Zhou, Y. Jin, and M. Gu, “Physical and photocatalytic properties of zinc ferrite doped titania under visible light irradiation,” *Journal of Photochemistry and Photobiology A: Chemistry*, vol. 168, no. 1-2, pp. 97–101, 2004.

[22] A. Du, Y. Ng, N. Bell, Z. Zhu, R. Amal, and S. Smith, “Hybrid graphene/titania nanocomposite: Interface charge transfer, hole doping, and sensitization for visible light response,” *Journal of Physical Chemistry Letters*, vol. 2, no. 8, pp. 894–899, 2011.

[23] M. Sher Shah, A. Park, K. Zhang, J. Park, and P. Yoo, “Green synthesis of biphasic $TiO_2$-reduced graphene oxide nanocomposites with highly enhanced photocatalytic activity,” *ACS Applied Materials and Interfaces*, vol. 4, no. 8, pp. 3893–3901, 2012.

[24] K. Lee, A. Mazare, and P. Schmuki, “One-dimensional titanium dioxide nanomaterials: Nanotubes,” *Chemical Reviews*, vol. 114, no. 19, pp. 9385–9454, 2014.

[25] T. Kasuga, M. Hiramatsu, A. Hoson, T. Sekino, and K. Niihara, “Formation of titanium oxide nanotube,” *Langmuir*, vol. 14, no. 12, pp. 3160–3163, 1998.

[26] T. Kasuga, M. Hiramatsu, A. Hoson, T. Sekino, and K. Niihara, “Titania nanotubes prepared by chemical processing,” *Advanced Materials*, vol. 11, no. 15, pp. 1307–1311, 1999.

[27] M. Sander, M. Côté, W. Gu, B. Kile, and C. Tripp, “Template-assisted fabrication of dense, aligned arrays of titania nanotubes with well-controlled dimensions on substrates,” *Advanced Materials*, vol. 16, no. 22, pp. 2052–2057, 2004.

[28] G. H. Du, Q. Chen, R. C. Che, Z. Y. Yuan, and L.-M. Peng, "Preparation and structure analysis of titanium oxide nanotubes," *Applied Physics Letters*, vol. 79, no. 22, pp. 3702–3704, 2001.

[29] E. Morgado, M. A. S. de Abreu, G. T. Moure, B. A. Marinkovic, P. M. Jardim, and A. S. Araujo, "Characterization of nanostructured titanates obtained by alkali treatment of $TiO_2$-anatases with distinct crystal sizes," *Chemistry of Materials*, vol. 19, no. 4, pp. 665–676, 2007.

[30] N. Wang, H. Lin, J. Li, L. Zhang, C. Lin, and X. Li, "Crystalline transition from $H_2Ti_3O_7$ nanotubes to anatase nanocrystallines under low-temperature hydrothermal conditions," *Journal of the American Ceramic Society*, vol. 89, no. 11, pp. 3564–3566, 2006.

[31] M. Zhang, Z. Jin, J. Zhang, X. Guo, J. Yang, W. Li, X. Wang, and Z. Zhang, "Effect of annealing temperature on morphology, structure and photocatalytic behavior of nanotubed $H_2Ti_2O_4(OH)_2$," *Journal of Molecular Catalysis A: Chemical*, vol. 217, no. 1, pp. 203 – 210, 2004.

[32] M. Qamar, C. R. Yoon, H. J. Oh, D. H. Kim, J. H. Jho, K. S. Lee, W. J. Lee, H. G. Lee, and S. J. Kim, "Effect of post treatments on the structure and thermal stability of titanate nanotubes," *Nanotechnology*, vol. 17, no. 24, p. 5922, 2006.

[33] T. Brunatova, D. Popelkova, W. Wan, P. Oleynikov, S. Danis, X. Zou, and R. Kuzel, "Study of titanate nanotubes by X-ray and electron diffraction and electron microscopy," *Materials Characterization*, vol. 87, pp. 166 – 171, 2014.

[34] Y. Wang, G. Hu, X. Duan, H. Sun, and Q. Xue, "Microstructure and formation mechanism of titanium dioxide nanotubes," *Chemical Physics Letters*, vol. 365, no. 5, pp. 427 – 431, 2002.

[35] N. H. Nguyen and H. Bai, "Effect of washing pH on the properties of titanate nanotubes and its activity for photocatalytic oxidation of NO and $NO_2$," *Applied Surface Science*, vol. 355, pp. 672 – 680, 2015.

[36] C.-K. Lee, C.-C. Wang, M.-D. Lyu, L.-C. Juang, S.-S. Liu, and S.-H. Hung, "Effects of sodium content and calcination temperature on the morphology, structure and photocatalytic activity of nanotubular titanates," *Journal of Colloid and Interface Science*, vol. 316, no. 2, pp. 562 – 569, 2007.

[37] V. Zwilling, E. Darque-Ceretti, A. Boutry-Forveille, D. David, M. Y. Perrin, and M. Aucouturier, "Structure and physicochemistry of anodic oxide films on titanium and TA6V alloy," *Surface and Interface Analysis*, vol. 27, no. 7, pp. 629–637, 1999.

[38] R. Beranek, H. Hildebrand, and P. Schmuki, "Self-organized porous titanium oxide prepared in $H_2SO_4$/HF electrolytes," *Electrochemical and Solid-State Letters*, vol. 6, no. 3, pp. B12–B14, 2003.

[39] A. Ghicov, H. Tsuchiya, J. M. Macak, and P. Schmuki, "Titanium oxide nanotubes prepared in phosphate electrolytes," *Electrochemistry Communications*, vol. 7, no. 5, pp. 505 – 509, 2005.

[40] J. M. Macák, H. Tsuchiya, and P. Schmuki, "High-aspect-ratio $TiO_2$ nanotubes by anodization of titanium," *Angewandte Chemie International Edition*, vol. 44, no. 14, pp. 2100–2102, 2005.

[41] J. M. Macak, H. Tsuchiya, L. Taveira, S. Aldabergerova, and P. Schmuki, "Smooth anodic $TiO_2$ nanotubes," *Angewandte Chemie International Edition*, vol. 44, no. 45, pp. 7463–7465, 2005.

[42] N. F. Fahim and T. Sekino, "A novel method for synthesis of titania nanotube powders using rapid breakdown anodization," *Chemistry of Materials*, vol. 21, no. 9, pp. 1967–1979, 2009.

[43] E. Moyen, L. Santinacci, L. Masson, W. Wulfhekel, and M. Hanbücken, "A novel self-ordered sub-10 nm nanopore template for nanotechnology," *Advanced Materials*, vol. 24, no. 37, pp. 5094–5098, 2012.

[44] A. Michailowski, D. AlMawlawi, G. Cheng, and M. Moskovits, "Highly regular anatase nanotubule arrays fabricated in porous anodic templates," *Chemical Physics Letters*, vol. 349, no. 1, pp. 1 – 5, 2001.

[45] M. Inagaki, N. Kondo, R. Nonaka, E. Ito, M. Toyoda, K. Sogabe, and T. Tsumura, "Structure and photoactivity of titania derived from nanotubes and nanofibers," *Journal of Hazardous Materials*, vol. 161, no. 2, pp. 1514 – 1521, 2009.

[46] L. Xiong, W. Sun, Y. Yang, C. Chen, and J. Ni, "Heterogeneous photocatalysis of methylene blue over titanate nanotubes: Effect of adsorption," *Journal of Colloid and Interface Science*, vol. 356, no. 1, pp. 211 – 216, 2011.

[47] C. Guo, J. Xu, Y. He, Y. Zhang, and Y. Wang, "Photodegradation of rhodamine B and methyl orange over one-dimensional $TiO_2$ catalysts under simulated solar irradiation," *Applied Surface Science*, vol. 257, no. 8, pp. 3798 – 3803, 2011.

[48] S. Chatterjee, A. Tyagi, and P. Ayyub, "Efficient photocatalytic degradation of rhodamine B dye by aligned arrays of self-assembled hydrogen titanate nanotubes," *Journal of Nanomaterials*, vol. 2014, 2014.

[49] Y. Liao, W. Que, P. Zhong, J. Zhang, and Y. He, "A facile method to crystallize amorphous anodized $TiO_2$ nanotubes at low temperature," *ACS Applied Materials & Interfaces*, vol. 3, no. 7, pp. 2800–2804, 2011.

[50] R. Hahn, M. Stark, M. S. Killian, and P. Schmuki, "Photocatalytic properties of in situ doped $TiO_2$-nanotubes grown by rapid breakdown anodization," *Catalysis Science & Technology*, vol. 3, pp. 1765–1770, 2013.

[51] Z. Hua, Z. Dai, X. Bai, Z. Ye, H. Gu, and X. Huang, "A facile one-step electrochemical strategy of doping iron, nitrogen, and fluorine into titania nanotube arrays with enhanced visible light photoactivity," *Journal of Hazardous Materials*, vol. 293, pp. 112 – 121, 2015.

[52] B. Réti, K. Mogyorósi, A. Dombi, and K. Hernádi, "Substrate dependent photocatalytic performance of $TiO_2$/MWCNT photocatalysts," *Applied Catalysis A: General*, vol. 469, pp. 153 – 158, 2014.

[53] R. Savitha, R. Raghunathan, and R. Chetty, "Rutile nanotubes by electrochemical anodization," *RSC Advances*, vol. 6, pp. 74510–74514, 2016.

[54] Y. R. Smith, R. S. Ray, K. Carlson, B. Sarma, and M. Misra, "Self-ordered titanium dioxide nanotube arrays: Anodic synthesis and their photo/electro-catalytic applications," *Materials*, vol. 6, no. 7, pp. 2892–2957, 2013.

[55] A. Ghicov, J. M. Macak, H. Tsuchiya, J. Kunze, V. Haeublein, L. Frey, and P. Schmuki, "Ion implantation and annealing for an efficient N-doping of $TiO_2$ nanotubes," *Nano Letters*, vol. 6, no. 5, pp. 1080–1082, 2006.

[56] T. M. David, P. Wilson, R. Mahesh, S. Dhanavel, S. Hussain, S. J. M. Boby, A. Stephen, C. Ramesh, and P. Sagayaraj, "Investigating the photocatalytic degradation property of Pt, Pd and Ni nanoparticles-loaded $TiO_2$ nanotubes powder prepared via rapid breakdown anodization," *Environmental Technology*, vol. 0, no. 0, pp. 1–12, 2017.

[57] D. Guerrero-Araque, D. Ramírez-Ortega, R. Gómez, and P. Acevedo-Peña, "Rapid breakdown anodization to obtain nanostructured $TiO_2$ powders for photocatalytic hydrogen generation," *Journal of Materials Science: Materials in Electronics*, vol. 28, no. 13, pp. 9859–9866, 2017.

[58] S. Sato, "Photocatalytic activity of $NO_2$-doped $TiO_2$ in the visible light region," *Chemical Physics Letters*, vol. 123, no. 1, pp. 126 – 128, 1986.

[59] H. Irie, Y. Watanabe, and K. Hashimoto, "Nitrogen-concentration dependence on photocatalytic activity of $TiO_2$-$xN_x$ powders," *Journal of Physical Chemistry B*, vol. 107, no. 23, pp. 5483–5486, 2003.

[60] M. Batzill, E. Morales, and U. Diebold, "Influence of nitrogen doping on the defect formation and surface properties of $TiO_2$ rutile and anatase," *Physical Review Letters*, vol. 96, no. 2, 2006.

[61] X. Chen and C. Burda, "The electronic origin of the visible-light absorption properties of C-, N- and S-doped $TiO_2$ nanomaterials," *Journal of the American Chemical Society*, vol. 130, no. 15, pp. 5018–5019, 2008.

[62] N. Nguyen, S. Ozkan, O. Tomanec, R. Zboril, and P. Schmuki, "Spaced titania nanotube arrays allow the construction of an efficient N-doped hierarchical structure for visible-light harvesting," *ChemistryOpen*, vol. 7, no. 2, pp. 131–135, 2018. cited By 0.

[63] Y. Wu, M. Xing, B. Tian, J. Zhang, and F. Chen, "Preparation of nitrogen and fluorine co-doped mesoporous $TiO_2$ microsphere and photodegradation of acid orange 7 under visible light," *Chemical Engineering Journal*, vol. 162, no. 2, pp. 710–717, 2010.

[64] K. Siuzdak, M. Szkoda, M. Sawczak, A. Lisowska-Oleksiak, J. Karczewski, and J. Ryl, "Enhanced photoelectrochemical and photocatalytic performance of iodine-doped titania nanotube arrays," *RSC Advances*, vol. 5, pp. 50379–50391, 2015.

[65] H. Xu, Z. Zheng, L. Zhang, H. Zhang, and F. Deng, "Hierarchical chlorine-doped rutile $TiO_2$ spherical clusters of nanorods: Large-scale synthesis and high photocatalytic activity," *Journal of Solid State Chemistry*, vol. 181, no. 9, pp. 2516–2522, 2008.

[66] P. Bouras, E. Stathatos, and P. Lianos, "Pure versus metal-ion-doped nanocrystalline titania for photocatalysis," *Applied Catalysis B: Environmental*, vol. 73, no. 1-2, pp. 51–59, 2007.

[67] J. Yu, G. Dai, and B. Huang, "Fabrication and characterization of visible-light-driven plasmonic photocatalyst Ag/AgCl/$TiO_2$ nanotube arrays," *Journal of Physical Chemistry C*, vol. 113, no. 37, pp. 16394–16401, 2009.

[68] S. Liu, Z. Qu, X. Han, and C. Sun, "A mechanism for enhanced photocatalytic activity of silver-loaded titanium dioxide," *Catalysis Today*, vol. 93-95, pp. 877 – 884, 2004. Selections from the presentations of the 3rd Asia-Pacific Congress on Catalysis.

[69] B. Xin, L. Jing, Z. Ren, B. Wang, and H. Fu, "Effects of simultaneously doped and deposited Ag on the photocatalytic activity and surface states of $TiO_2$," *The Journal of Physical Chemistry B*, vol. 109, no. 7, pp. 2805–2809, 2005.

[70] T. Lambert, C. Chavez, B. Hernandez-Sanchez, P. Lu, N. Bell, A. Ambrosini, T. Friedman, T. Boyle, D. Wheeler, and D. Huber, "Synthesis and characterization of titania-graphene nanocomposites," *Journal of Physical Chemistry C*, vol. 113, no. 46, pp. 19812–19823, 2009.

[71] V. Štengl, D. Popelková, and P. Vláčil, "$TiO_2$-graphene nanocomposite as high performace photocatalysts," *Journal of Physical Chemistry C*, vol. 115, no. 51, pp. 25209–25218, 2011.

[72] W. Wang, J. Yu, Q. Xiang, and B. Cheng, "Enhanced photocatalytic activity of hierarchical macro/mesoporous $TiO_2$-graphene composites for photodegradation of acetone in air," *Applied Catalysis B: Environmental*, vol. 119-120, pp. 109–116, 2012.

[73] A. Anshuman, S. Saremi-Yarahmadi, and B. Vaidhyanathan, "Enhanced catalytic performance of reduced graphene oxide-$TiO_2$ hybrids for efficient water treatment using microwave irradiation," *RSC Advances*, vol. 8, no. 14, pp. 7709–7715, 2018.

[74] A. Geim and K. S. Novoselov, "The rise of graphene," *Nature Materials*, vol. 6, pp. 183–191, 2007.

[75] W. S. Hummers and R. E. Offeman, "Preparation of graphitic oxide," *Journal of the American Chemical Society*, vol. 80, no. 6, pp. 1339–1339, 1958.

[76] N. I. Kovtyukhova, P. J. Ollivier, B. R. Martin, T. E. Mallouk, S. A. Chizhik, E. V. Buzaneva, and A. D. Gorchinskiy, "Layer-by-layer assembly of ultrathin composite films from micron-sized graphite oxide sheets and polycations," *Chemistry of Materials*, vol. 11, no. 3, pp. 771–778, 1999.

[77] S. D. Perera, R. G. Mariano, K. Vu, N. Nour, O. Seitz, Y. Chabal, and K. J. Balkus, "Hydrothermal Synthesis of Graphene-$TiO_2$ Nanotube Composites with Enhanced Photocatalytic Activity," *ACS Catalysis*, vol. 2, no. 6, pp. 949–956, 2012.

[78] Y. Wen, H. Ding, and Y. Shan, "Preparation and visible light photocatalytic activity of Ag/$TiO_2$/graphene nanocomposite," *Nanoscale*, vol. 3, pp. 4411–4417, 2011.

[79] M. S. Arif Sher Shah, K. Zhang, A. R. Park, K. S. Kim, N.-G. Park, J. H. Park, and P. J. Yoo, "Single-step solvothermal synthesis of mesoporous Ag-$TiO_2$-reduced graphene oxide ternary composites with enhanced photocatalytic activity," *Nanoscale*, vol. 5, pp. 5093–5101, 2013.

[80] L. Liu, H. Bai, J. Liu, and D. D. Sun, "Multifunctional graphene oxide-$TiO_2$-Ag nanocomposites for high performance water disinfection and decontamination under solar irradiation," *Journal of Hazardous Materials*, vol. 261, pp. 214 – 223, 2013.

[81] Y. Xie and Y. Meng, "SERS performance of graphene oxide decorated silver nanoparticle/titania nanotube array," *RSC Advances*, vol. 4, pp. 41734–41743, 2014.

[82] W. Gao, M. Wang, C. Ran, X. Yao, H. Yang, J. Liu, D. He, and J. Bai, "One-pot synthesis of Ag/r-GO/$TiO_2$ nanocomposites with high solar absorption and enhanced anti-recombination in photocatalytic applications," *Nanoscale*, vol. 6, pp. 5498–5508, 2014.

[83] E. Vasilaki, I. Georgaki, D. Vernardou, M. Vamvakaki, and N. Katsarakis, "Ag-loaded $TiO_2$/reduced graphene oxide nanocomposites for enhanced visible-light photocatalytic activity," *Applied Surface Science*, vol. 353, pp. 865 – 872, 2015.

[84] T.-L. Guo, J.-G. Li, X. Sun, and Y. Sakka, "Photocatalytic growth of Ag nanocrystals on hydrothermally synthesized multiphasic $TiO_2$/reduced graphene oxide (rGO) nanocomposites and their SERS performance," *Applied Surface Science*, vol. 423, pp. 1–12, 2017.

[85] P. Wang, Y. Tang, Z. Dong, Z. Chen, and T.-T. Lim, "Ag-AgBr/$TiO_2$/RGO nanocomposite for visible-light photocatalytic degradation of penicillin G," *Journal of Materials Chemistry A*, vol. 1, no. 15, pp. 4718–4727, 2013.

[86] H. Pan, X. Zhao, Z. Fu, W. Tu, P. Fang, and H. Zhang, "Visible-light induced photocatalysis of AgCl@Ag/titanate nanotubes/nitrogen-doped reduced graphite oxide composites," *Applied Surface Science*, vol. 442, pp. 547–555, 2018.

[87] "Dictionary.com unabridged," Feb 2018.

[88] J. Jiménez, M. Sendova, T. Hartsfield, and M. Sendova-Vassileva, "In situ optical microspectroscopy of the growth and oxidation of silver nanoparticles in silica thin films on soda-lime glass," *Materials Research Bulletin*, vol. 46, no. 2, pp. 158 – 165, 2011.

[89] W. Wan, J. Luo, J. Yang, Y. Feng, Y. Ouyang, D. Chen, and T. Qiu, "High-temperature ablation properties of nano zirconia reinforced fused silica ceramics," *Ceramics International*, vol. 44, no. 6, pp. 7273–7275, 2018.

[90] Y. Chen, C. Zuo, X. Ma, and A. Chen, "Solid-silica core/mesoporous-silica shell composite abrasives: synthesis, characterization, and the effect of mesoporous shell structures on cmp," *Journal of Materials Science: Materials in Electronics*, vol. 29, no. 5, pp. 3817–3828, 2018.

[91] I. Slowing, J. Vivero-Escoto, C.-W. Wu, and V.-Y. Lin, "Mesoporous silica nanoparticles as controlled release drug delivery and gene transfection carriers," *Advanced Drug Delivery Reviews*, vol. 60, no. 11, pp. 1278–1288, 2008.

[92] K. Straif, L. Benbrahim-Tallaa, R. Baan, Y. Grosse, B. Secretan, F. El Ghissassi, V. Bouvard, N. Guha, C. Freeman, L. Galichet, and V. Cogliano, "A review of human carcinogens–part c: metals, arsenic, dusts, and fibres.," *The Lancet Oncology*, vol. 10, no. 5, pp. 453–454, 2009.

[93] Y. Wang, Q. Zhao, N. Han, L. Bai, J. Li, J. Liu, E. Che, L. Hu, Q. Zhang, T. Jiang, and S. Wang, "Mesoporous silica nanoparticles in drug delivery and biomedical applications," *Nanomedicine: Nanotechnology, Biology and Medicine*, vol. 11, no. 2, pp. 313 – 327, 2015.

[94] W. Stöber, A. Fink, and E. Bohn, "Controlled growth of monodisperse silica spheres in the micron size range," *Journal of Colloid and Interface Science*, vol. 26, no. 1, pp. 62–69, 1968.

[95] Y. Kobayashi, H. Katakami, E. Mine, D. Nagao, M. Konno, and L. M. Liz-Marzán, "Silica coating of silver nanoparticles using a modified Stöber method," *Journal of Colloid and Interface Science*, vol. 283, no. 2, pp. 392 – 396, 2005.

[96] F. Furno, K. S. Morley, B. Wong, B. L. Sharp, P. L. Arnold, S. M. Howdle, R. Bayston, P. D. Brown, P. D. Winship, and H. J. Reid, "Silver nanoparticles and polymeric medical devices: a new approach to prevention of infection?," *Journal of Antimicrobial Chemotherapy*, vol. 54, no. 6, pp. 1019–1024, 2004.

[97] S. Chernousova and M. Epple, "Silver as antibacterial agent: Ion, nanoparticle, and metal," *Angewandte Chemie International Edition*, vol. 52, no. 6, pp. 1636–1653, 2013.

[98] S. Prabhu and E. K. Poulose, "Silver nanoparticles: mechanism of antimicrobial action, synthesis, medical applications, and toxicity effects," *International Nano Letters*, vol. 2, p. 32, Oct 2012.

[99] J. S. Kim, E. Kuk, K. N. Yu, J.-H. Kim, S. J. Park, H. J. Lee, S. H. Kim, Y. K. Park, Y. H. Park, C.-Y. Hwang, Y.-K. Kim, Y.-S. Lee, D. H. Jeong, and M.-H. Cho, "Antimicrobial effects of silver nanoparticles," *Nanomedicine: Nanotechnology, Biology and Medicine*, vol. 3, no. 1, pp. 95 – 101, 2007.

[100] Q. Feng, J. Wu, G. Chen, F. Cui, T. Kim, and J. Kim, "A mechanistic study of the antibacterial effect of silver ions on Escherichia coli and Staphylococcus aureus," *Journal of Biomedical Materials Research*, vol. 52, no. 4, pp. 662–668, 2000.

[101] S. Agnihotri, S. Mukherji, and S. Mukherji, "Size-controlled silver nanoparticles synthesized over the range 5-100 nm using the same protocol and their antibacterial efficacy," *RSC Advances*, vol. 4, pp. 3974–3983, 2014.

[102] D. M. Ledwith, A. M. Whelan, and J. M. Kelly, "A rapid, straight-forward method for controlling the morphology of stable silver nanoparticles," *Journal of Materials Chemistry*, vol. 17, pp. 2459–2464, 2007.

[103] L. Tzounis, R. Contreras-Caceres, L. Schellkopf, D. Jehnichen, D. Fischer, C. Cai, P. Uhlmann, and M. Stamm, "Controlled growth of Ag nanoparticles decorated onto the surface of $SiO_2$ spheres: a nanohybrid system with combined SERS and catalytic properties," *RSC Advances*, vol. 4, pp. 17846–17855, 2014.

[104] Y. Zhou, S. H. Yu, X. P. Cui, C. Y. Wang, and Z. Y. Chen, "Formation of silver nanowires by a novel solid-liquid phase arc discharge method," *Chemistry of Materials*, vol. 11, no. 3, pp. 545–546, 1999.

[105] Y. Zhou, S. Yu, C. Wang, X. Li, Y. Zhu, and Z. Chen, "A novel ultraviolet irradiation photoreduction technique for the preparation of single-crystal Ag nanorods and Ag dendrites," *Advanced Materials*, vol. 11, no. 10, pp. 850–852, 1999.

[106] N. A. Kotov, M. E. D. Zaniquelli, F. C. Meldrum, and J. H. Fendler, "Two-dimensional silver electrocrystallization under monolayers spread on aqueous silver nitrate," *Langmuir*, vol. 9, no. 12, pp. 3710–3716, 1993.

[107] N. M. Bahadur, T. Furusawa, M. Sato, F. Kurayama, I. A. Siddiquey, and N. Suzuki, "Fast and facile synthesis of silica coated silver nanoparticles by microwave irradiation," *Journal of Colloid and Interface Science*, vol. 355, no. 2, pp. 312 – 320, 2011.

[108] K.-Y. Pan, Y.-F. Liang, Y.-C. Pu, Y.-J. Hsu, J.-W. Yeh, and H. C. Shih, "Studies on the photocatalysis of core-shelled $SiO_2$–Ag nanospheres by controlled surface plasmon resonance under visible light," *Applied Surface Science*, vol. 311, pp. 399 – 404, 2014.

[109] T. Liu, D. Li, D. Yang, and M. Jiang, "An improved seed-mediated growth method to coat complete silver shells onto silica spheres for surface-enhanced Raman scattering," *Colloids and Surfaces A: Physicochemical and Engineering Aspects*, vol. 387, no. 1, pp. 17 – 22, 2011.

[110] M. Liong, B. France, K. A. Bradley, and J. I. Zink, "Antimicrobial activity of silver nanocrystals encapsulated in mesoporous silica nanoparticles," *Advanced Materials*, vol. 21, no. 17, pp. 1684–1689, 2009.

[111] S. Kaya, M. Cresswell, and A. R. Boccaccini, "Mesoporous silica-based bioactive glasses for antibiotic-free antibacterial applications," *Materials Science and Engineering: C*, vol. 83, pp. 99 – 107, 2018.

[112] K. Xu, J.-X. Wang, X.-L. Kang, and J.-F. Chen, "Fabrication of antibacterial monodispersed Ag–$SiO_2$ core–shell nanoparticles with high concentration," *Materials Letters*, vol. 63, no. 1, pp. 31 – 33, 2009.

[113] Q. Cai, W.-Y. Lin, F.-S. Xiao, W.-Q. Pang, X.-H. Chen, and B.-S. Zou, "The preparation of highly ordered MCM-41 with extremely low surfactant concentration," *Microporous and Mesoporous Materials*, vol. 32, no. 1, pp. 1 – 15, 1999.

[114] D. V. Quang, P. B. Sarawade, A. Hilonga, S. D. Park, J.-K. Kim, and H. T. Kim, "Facile route for preparation of silver nanoparticle-coated precipitated silica," *Applied Surface Science*, vol. 257, no. 9, pp. 4250 – 4256, 2011.

[115] S. Egger, R. Lehmann, M. Height, M. Loessner, and M. Schuppler, "Antimicrobial properties of a novel silver-silica nanocomposite material," *Applied and Environmental Microbiology*, vol. 75, no. 9, pp. 2973–2976, 2009.

[116] D. Church, S. Elsayed, O. Reid, B. Winston, and R. Lindsay, "Burn wound infections," *Clinical Microbiology Reviews*, vol. 19, no. 2, pp. 403–434, 2006.

[117] E. Haimi, H. Lipsonen, J. Larismaa, M. Kapulainen, J. Krzak-Ros, and S.-P. Hannula, "Optical and structural properties of nanocrystalline anatase ($TiO_2$) thin films prepared by non-aqueous sol-gel dip-coating," *Thin Solid Films*, vol. 519, no. 18, pp. 5882 – 5886, 2011.

[118] J. Larismaa, T. Honkanen, Y. Ge, O. Söderberg, M. Friman, and S.-P. Hannula, "Effect of annealing on ag-doped submicron silica powder prepared with modified stöber method," *Materials Science Forum*, vol. 695, pp. 449–452, 2011.

[119] J. Yang, Z. Jin, X. Wang, W. Li, J. Zhang, S. Zhang, X. Guo, and Z. Zhang, "Study on composition, structure and formation process of nanotube $Na_2Ti_2O_4(OH)_2$," *Dalton Transactions*, pp. 3898–3901, 2003.

[120] B. Poudel, W. Wang, C. Dames, J. Huang, S. Kunwar, D. Wang, D. Banerjee, G. Chen, and Z. Ren, "Formation of crystallized titania nanotubes and their transformation into nanowires," *Nanotechnology*, vol. 16, no. 9, pp. 1935–1940, 2005.

[121] H.-H. Ou and S.-L. Lo, "Review of titania nanotubes synthesized via the hydrothermal treatment: Fabrication, modification, and application," *Separation and Purification Technology*, vol. 58, no. 1, pp. 179 – 191, 2007. Application of Nanotechnologies in Separation and Purification.

[122] H. Yan, X. Tao, Z. Yang, K. Li, H. Yang, A. Li, and R. Cheng, "Effects of the oxidation degree of graphene oxide on the adsorption of methylene blue," *Journal of Hazardous Materials*, vol. 268, pp. 191 – 198, 2014.

[123] W. Zhang, C. Zhou, W. Zhou, A. Lei, Q. Zhang, Q. Wan, and B. Zou, "Fast and considerable adsorption of methylene blue dye onto graphene oxide," *Bulletin of Environmental Contamination and Toxicology*, vol. 87, no. 1, p. 86, 2011.

[124] J. Feng, J. Zhu, W. Lv, J. Li, and W. Yan, "Effect of hydroxyl group of carboxylic acids on the adsorption of Acid Red G and Methylene Blue on $TiO_2$," *Chemical Engineering Journal*, vol. 269, pp. 316 – 322, 2015.

[125] A. Sandoval, C. Hernández-Ventura, and T. E. Klimova, "Titanate nanotubes for removal of methylene blue dye by combined adsorption and photocatalysis," *Fuel*, vol. 198, pp. 22 – 30, 2017. International Mexican Congress on Chemical Reaction Engineering (IMCCRE 2016).

[126] K. Kiatkittipong and S. Assabumrungrat, "A comparative study of sodium/hydrogen titanate nanotubes/nanoribbons on destruction of recalcitrant compounds and sedimentation," *Journal of Cleaner Production*, vol. 148, pp. 905 – 914, 2017.

[127] M. N. Subramaniam, P. S. Goh, N. Abdullah, W. J. Lau, B. C. Ng, and A. F. Ismail, "Adsorption and photocatalytic degradation of methylene blue using high surface area titanate nanotubes (TNT) synthesized via hydrothermal method," *Journal of Nanoparticle Research*, vol. 19, no. 6, p. 220, 2017.

[128] J. M. Byun, H. R. Choi, Y. D. Kim, T. Sekino, and S. H. Kim, "Photocatalytic activity under UV/Visible light range of Nb-doped titanate nanostructures synthesized with Nb oxide," *Applied Surface Science*, vol. 415, pp. 126 – 131, 2017. 14th International Symposium on Novel and Nano Materials.

[129] X. Luan, M. T. G. Wing, and Y. Wang, "Enhanced photocatalytic activity of graphene oxide/titania nanosheets composites for methylene blue degradation," *Materials Science in Semiconductor Processing*, vol. 30, pp. 592 – 598, 2015.

[130] H. M. Yadav and J.-S. Kim, "Solvothermal synthesis of anatase $TiO_2$-graphene oxide nanocomposites and their photocatalytic performance," *Journal of Alloys and Compounds*, vol. 688, pp. 123 – 129, 2016.

[131] P. Wang, B. Huang, X. Qin, X. Zhang, Y. Dai, J. Wei, and M.-H. Whangbo, "Ag@AgCl: A Highly Efficient and Stable Photocatalyst Active under Visible Light," *Angewandte Chemie International Edition*, vol. 47, no. 41, pp. 7931–7933, 2008.

[132] C. J. Miller, H. Yu, and T. Waite, "Degradation of rhodamine B during visible light photocatalysis employing Ag@AgCl embedded on reduced graphene oxide," *Colloids and Surfaces A: Physicochemical and Engineering Aspects*, vol. 435, pp. 147 – 153, 2013. Special Issue : IAP 2012.

[133] T. Watanabe, T. Takizawa, and K. Honda, "Photocatalysis through excitation of adsorbates. 1. Highly efficient N-deethylation of rhodamine B adsorbed to cadmium sulfide," *The Journal of Physical Chemistry*, vol. 81, no. 19, pp. 1845–1851, 1977.

[134] Y. Ma and J. nian Yao, "Photodegradation of Rhodamine B catalyzed by $TiO_2$ thin filmsa," *Journal of Photochemistry and Photobiology A: Chemistry*, vol. 116, no. 2, pp. 167 – 170, 1998.

[135] D. Ila, J. Baglin, and R. Zimmerman, "Nano-Crystal Formation and Growth from High-Fluence Ion Implantation of Au, Ag or Cu in Silica," *Physics Procedia*, vol. 66, pp. 548 – 555, 2015. The 23rd International Conference on the Application of Accelerators in Research and Industry - CAARI 2014.

[136] J. Jiménez, M. Sendova, and H. Liu, "Evolution of the optical properties of a silver-doped phosphate glass during thermal treatment," *Journal of Luminescence*, vol. 131, no. 3, pp. 535 – 538, 2011. Selected papers from DPC'10.

[137] J. Jiménez and M. Sendova, "Diffusion activation energy of ag in nanocomposite glasses determined by in situ monitoring of plasmon resonance evolution," *Chemical Physics Letters*, vol. 503, no. 4, pp. 283 – 286, 2011.

[138] Y. Tian, J. Qi, W. Zhang, Q. Cai, and X. Jiang, "Facile, one-pot synthesis, and antibacterial activity of mesoporous silica nanoparticles decorated with well-dispersed silver nanoparticles," *ACS Applied Materials & Interfaces*, vol. 6, no. 15, pp. 12038–12045, 2014.

[139] D. Leaper, "Appropriate use of silver dressings in wounds: International consensus document," *International Wound Journal*, vol. 9, no. 5, pp. 461–464, 2012.

[140] M. Yamanaka, K. Hara, and J. Kudo, "Bactericidal actions of a silver ion solution on Escherichia coli, studied by energy-filtering transmission electron microscopy and proteomic analysis," *Applied and Environmental Microbiology*, vol. 71, no. 11, pp. 7589–7593, 2005.

# Errata

### Publication IV

The caption for Figure 2 should be: *"X-ray diffraction patterns of* $SiO_2$*-Ag powders heat treated at (a) 300 °C; (b) 400 °C; (c) 500 °C; (d) 600 °C; (e) 700 °C and (f) 800 °C for 75 min."* A citation for reference [12] was omitted from Figure 4b.

Aalto-DD 159/2018

ISBN 978-952-60-8145-8 (printed)
ISBN 978-952-60-8146-5 (pdf)
ISSN 1799-4934 (printed)
ISSN 1799-4942 (pdf)

**Aalto University**
**School of Chemical Engineering**
**Department of Chemistry and Materials Science**
**www.aalto.fi**

BUSINESS +
ECONOMY

ART +
DESIGN +
ARCHITECTURE

SCIENCE +
TECHNOLOGY

CROSSOVER

**DOCTORAL**
**DISSERTATIONS**